On the Particle Formation of Leucine in Spray Drying of Inhalable Microparticles

Mani Ordoubadi[1], Florence K. A. Gregson[2], Hui Wang[1], Mark Nicholas[3], Sandra Gracin[3], David

Lechuga-Ballesteros[4], Jonathan P. Reid[2], Warren H. Finlay[1], Reinhard Vehring[1,*]

[1]Department of Mechanical Engineering, University of Alberta, Edmonton, Alberta, Canada

[2]School of Chemistry, University of Bristol, Bristol, United Kingdom

[3]Inhalation Product Development, Pharmaceutical Technology & Development, Operations, AstraZeneca, Gothenburg, Sweden

[4]Inhalation Product Development, Pharmaceutical Technology & Development, Operations, AstraZeneca, South San Francisco,

California, USA

Corresponding author:

Reinhard Vehring

University of Alberta, Department of Mechanical Engineering, 10-203 Donadeo Innovation Centre for

Engineering, 9211 116th Street NW, Edmonton, Alberta T6G 1H9, Canada

reinhard.vehring@ualberta.ca

List of Chemical Compounds in this Study

Compound 1:

L-leucine

CAS# 61-90-5

Compound 2:

D-(+)-trehalose dihydrate

CAS# 6138-23-4

Abstract

The particle formation of L-leucine, a dispersibility-enhancing amino acid used in the spray drying of

inhalable pharmaceutical aerosols, was extensively studied using three experimental methods, and the

results were interpreted with the aid of theory. A comparative-kinetics electrodynamic balance was used

to study the shell formation behavior in single evaporating microdroplets containing leucine and

trehalose. Different concentration thresholds of solidification and shell formation were determined for

trehalose and leucine, which were then used in the particle formation model to predict the properties of

spray-dried particles. Furthermore, a droplet chain instrument was used to study the particle morphologies

and particle densities that were not accessible in the single particle experiments. Lab-scale spray drying

was also used to produce powders typical for actual pharmaceutical applications. Raman spectroscopy

confirmed that a glass former, such as trehalose, can inhibit the crystallization of leucine. The surface

compositions of these spray-dried powders were analyzed via time-of-flight secondary ion mass

spectrometry. The leucine surface coverage in a polydisperse powder was determined to be a function of

39   the particle size or the initial droplet diameter of each respective particle. This observation confirms the

40   important role of leucine crystallization kinetics in its shell-forming capabilities. A critical supersaturation

41   ratio of 3.5 was also calculated for leucine, at which it is assumed to instantaneously nucleate out of

42   solution. This ratio was used as the threshold for the initiation of crystallization. Crystallinity predictions

43   for the leucine-trehalose particles based on this supersaturation ratio were in good agreement with the

44   solid-state characterizations obtained by Raman spectroscopy. This study improves the fundamental

45   understanding of the particle formation process of leucine-containing formulations, which can apply to

46   other crystallizing systems and potentially facilitate the rational design of such formulations with reduced

47   experimental effort.

48

51

1. Introduction

53   Spray drying is a scalable industrial process that evaporates an atomized spray of a solution, a suspension

54   or an emulsion into a solid powder with a well-controlled size distribution. In the pharmaceutical

55   industry, spray drying has been used extensively in manufacturing solid dosage forms intended for

56   pulmonary delivery. An aerosol needs to have specific aerodynamic properties for successful delivery to

57   the intended areas of the lungs. Larger particles tend to deposit in the delivery device or the mouth-throat

58   region due to inertial impaction, while very small particles might be exhaled (Finlay, 2019). For efficient

59   delivery to the lungs, particles need to have aerodynamic diameters between approximately 1 and 5 µm

60   (Dabbagh et al., 2018). Therefore, particle deaggregation is an important stage in the passive or active

61   delivery of dry powder to the lungs, because an agglomerate behaves aerodynamically much like larger

62   particles and might not reach the targeted pulmonary site (Healy et al., 2014; Lechanteur and Evrard,

63   2020). To assist with the aerosolization of the particles, dispersibility-enhancing agents have been used in

64   spray drying of inhalable pharmaceutical aerosols. These materials operate in part by decreasing the

65   surface energy and increasing the surface rugosity and roughness of the particles and hence decreasing

66   inter-particle cohesion. It has been shown that increasing particle roughness reduces the cohesive forces

67   between particles due to reduction in their effective contact area (Baldelli and Vehring, 2016a; Wang et

68   al., 2019); while a reduction in surface energy directly reduces the cohesive forces (Lechuga-Ballesteros

69   et al., 2008).

70   L-leucine, an essential amino acid, has been widely used and studied as a dispersibility enhancer of spray-

71   dried inhalable microparticles (Boraey et al., 2013; Eedara et al., 2018; Li et al., 2016; Seville et al.,

72   2007). Leucine is a moderately surface-active material, compared to the stronger dispersibility enhancer

73   trileucine (Gliński et al., 2000; Lechuga-Ballesteros et al., 2008; Wang et al., 2019), and has relatively

74   low aqueous solubility, 22 mg/ml at room temperature (Li et al., 2016). These characteristics result in

75   rugose spray-dried particles with low surface energies, which contribute to lower interparticle cohesion

76   and thereby good aerosol performance (Lechuga-Ballesteros et al., 2019). Besides the dispersibility

77   enhancement, it has been shown that a crystalline leucine barrier can also reduce moisture uptake and

78   enhance aerosol performance in humid conditions (Li et al., 2016; Mah et al., 2019). These desirable

79   effects are direct consequences of the surface morphology and surface composition of the particles

80   containing leucine (Eedara et al., 2018; Li et al., 2016), which can to some extent be predicted from

81   surface rheology properties (Nuzzo et al., 2015) and particle formation models (Vehring, 2008). Based on

82   these observations, the utilization of leucine as an excipient in spray drying inhalable particles is

83   beneficial for different respirable dosage forms, such as colloidal suspensions in pressurized metered-dose

84   inhalers (Yang et al., 2015) and in dry powder inhalers (Eedara et al., 2018).

85   The fundamental understanding of the particle formation of leucine-containing formulations facilitates the

86   rational design of such powders with minimal experimental effort. Available particle formation models

87   can approximate the relative radial distribution of each component in an evaporating droplet and predict

4

88 the general morphology of the resulting spray-dried particles in single-solvent (Boraey and Vehring,

89 2014; Vehring et al., 2007) and multi-solvent formulations (Ordoubadi et al., 2019). The approximation is

90 relatively straightforward for non-surface-active materials and those which do not crystallize during spray

91 drying, such as most polysaccharides and polymers. However, leucine can crystallize during spray drying

92 (Feng et al., 2011), which complicates the prediction of the final particle morphology and the surface

93 composition of multi-component systems. This is because, upon nucleation and crystal growth, modelling

94 of the distribution of different components inside the droplet becomes difficult due to rapid changes in

95 their diffusion coefficients and because nucleation and crystal growth kinetics are not captured in the

96 available models.

97 To predict the onset of phase separation, precipitation or shell formation, particle formation models

98 compare the maximum concentration of each component inside the droplet, which is generally reached on

99 the surface of an evaporating droplet, to some predetermined value (Boraey and Vehring, 2014). For a

100 crystalline material, the solubility value is often considered as this limit, after which crystallization can

101 commence; while for an amorphous component, the concentration at which precipitation occurs is

102 compared to the true density of the material. For multicomponent amorphous systems, the total

103 concentration of the amorphous material can be compared to the true density of the amorphous mixture

104 (Carrigy et al., 2019). Nevertheless, the solidification does not happen exactly upon reaching these limits

105 (Vehring, 2008). For each specific system, further experimental observations are required to explain the

106 particle formation process. For example, for a crystallizing component, such as leucine, a critical

107 supersaturation is required for nucleation, which is a function of different chemical properties of the

108 participating molecules and the process parameters (He et al., 2006). Even if a value for a critical

109 supersaturation can be determined theoretically, the modeling of the ensuing phenomena such as the rate

110 of nucleation, crystal growth, and the subsequent surface enrichment of these crystallites is complicated

111 by the fact that they likely occur in highly supersaturated solutions due to the fast evaporation of

112   microdroplets in spray dryers (Baldelli et al., 2016). Hence, experimental investigation is essential to

113   better understand the particle formation in such systems.

114   Different experimental techniques have been used to study the drying kinetics of droplets containing

115   solidifying or crystallizing components. For example, the drying behavior of single droplets, usually in

116   the millimeter range, suspended from thin filaments has been studied (Fu et al., 2012). In this method, the

117   droplet is placed in a controlled environment with specified temperature and relative humidity. The

118   drying kinetics can be accurately measured via either an imaging technique or attachment of the thin

119   filament to a microbalance. The intrusive presence of the filament has been reported to affect the heat and

120   mass transfer between the environment and the droplet (de Souza Lima et al., 2020; Fu et al., 2012). In

121   another class of techniques used in such studies, single droplets have been successfully levitated using

122   acoustic forces (Griesing et al., 2016; Mondragon et al., 2011), drag forces induced by an air stream

123   (Hennet et al., 2011; Weber et al., 2016), the Leidenfrost effect (Marty and Tsapis, 2008) and

124   electrodynamic forces (Gregson et al., 2020, 2019; Ordoubadi et al., 2018). In these methods, the

125   environment conditions can be controlled easily, and the instantaneous size of the droplets can be

126   measured accurately, as the single droplets are usually held in place in a stable condition. The main

127   disadvantage of these methods is that the dried particle cannot be collected for any subsequent analysis. A

128   chain of falling monodisperse droplets has also been used to mimic the actual spray drying conditions to

129   some extent (Baldelli et al., 2016, 2015; Baldelli and Vehring, 2016b; Ordoubadi et al., 2019; Vehring et

130   al., 2007). In this method, usually called "the monodisperse droplet chain technique", the final dried

131   particles were collected to study their morphology using electron microscopy. However, the small

132   quantity of collected particles was not enough to allow other measurements such as Raman spectroscopy,

133   which requires milligrams of powder. Also, the inherent instability of the droplet chain can make accurate

134   measurement of the droplet size difficult, particularly in micrometer-size ranges. Although these

135   experimental tools are promising for the study of the drying kinetics of droplets and provide insights into

136   the particle formation processes, none of them represents actual spray drying conditions such as

137 polydispersity of the powder and the temperature and relative humidity variations in the spray plume.

138 Also, previous methodologies do not provide enough powder for a broad range of characterization

139 techniques. Consequently and not surprisingly, actual spray drying on laboratory-scale dryers is still a

140 popular method used in studying the particle formation of inhalable pharmaceutical aerosols (Eedara et

141 al., 2018; Mah et al., 2019; Mangal et al., 2015). The downside of lab-scale spray drying is that the drying

142 kinetics and the exact initial droplet size distributions cannot be measured directly, and the drying

143 conditions for the droplets are much less controlled.

144 In this study a theoretical model was compared to results from three experimental techniques: a single-

145 particle electrodynamic balance, a droplet chain instrument and a lab-scale spray dryer, in order to

146 overcome their individual limitations. The particle formation of leucine was studied in combination with a

147 disaccharide, trehalose. Trehalose was chosen as a model excipient for a glass stabilizer of biologics and

148 other active pharmaceutical ingredients (Carrigy et al., 2019; Feng et al., 2011; Lechuga-Ballesteros et al.,

149 2019).

150

2. Materials and Methods

151

2.1.   Materials

152

153 Different solutions of L-leucine (Cat. No. BP385-100, Fisher Scientific, Ottawa, ON, Canada) with D-

154 (+)-trehalose dihydrate (Cat. No. BP2687-1, Fisher Scientific, Ottawa, ON, Canada) were prepared using

155 HPLC-grade water (Cat. No. W5-4, Fisher Scientific, Ottawa, ON, Canada). The total excipient

156 concentrations were varied in the range of 5 to 50 mg/ml with different mass fractions of trehalose and

157 leucine.

158

159   2.2.   Experimental Investigation of Particle Formation

160   Three different experimental techniques were used for this study. A single-particle analysis was

161   performed using a Comparative-Kinetics Electrodynamic Balance (CK-EDB); in which single aerosol

162   droplets were levitated in a controlled environment to measure their size and to infer their general

163   morphology using scattered light (Gregson et al., 2019; Haddrell et al., 2019). Using this method, the

164   exact time and diameter at solidification can be determined accurately, enabling the estimation of the

165   critical point for shell formation for each formulation. To study the morphology of the resulting

166   microparticles using electron microscopy and to find the particle densities, a monodisperse droplet chain

167   instrument was used to collect dried particles. The initial droplet diameters in both of these instruments

168   (EDB: ~ 50 µm, droplet chain: ~ 40 µm) were larger than the typical sizes encountered in actual

169   pharmaceutical spray dryers of about 10 µm. To generalize the results to practical applications and to

170   produce enough powder for different characterization methods, a laboratory-scale spray dryer was used to

171   produce bulk powders in the respirable range (1-5 µm aerodynamic diameter).

172

173   2.2.1.   Comparative-Kinetics Electrodynamic Balance (CK-EDB)

174   The drying and solidification of single aerosol droplets in the form of aqueous solutions of the excipients

175   were studied using a CK-EDB (Davies et al., 2012). A single droplet (~50 µm diameter) was generated

176   using a droplet-on-demand dispenser (MJ-ABP-01, MicroFab Technologies, Plano, Texas, USA) and

177   charged by ion imbalance using DC voltage applied to an induction electrode positioned close to the tip of

178   the dispenser. The droplet was then trapped inside a temperature- and RH-controlled environment at the

179   center of the electrodynamic field, generated by applying an AC potential difference to two sets of

180   concentric cylindrical electrodes mounted vertically opposite one another. An additional DC voltage was

181   applied to the lower electrodes to counteract the gravitational force on the droplet. This electrodynamic

182   field was dynamically manipulated to account for the changes in droplet mass. Upon confinement of the

183   droplet in the trap, a 532 nm CW laser illuminated the particle. The interference between the reflected and

refracted light produced an elastically scattered pattern also known as the phase function. The phase function was captured every ~10 ms using a CCD sensor at a forward-scattering angle of 45° over an angular range of about 24°. The collected phase functions were then compared to Mie theory calculations to determine the size of the droplet at each time-point with an accuracy of ±100 nm (Gregson et al., 2019). The approximate morphology of the droplet during drying was also determined using a novel method based on the irregularities observed in the phase function (Haddrell et al., 2019). The different morphologies detected are homogeneous and spherical, spherical with inclusions, core-shell with high radial concentration gradients, and non-spherical or inhomogeneous. The instance of shell formation or solidification was determined for each case using these measured qualitative morphology data as well as deviations from constant-rate evaporation. Further details and technical information pertaining to this instrument can be found in previous publications (Gregson et al., 2019; Haddrell et al., 2019; Rovelli et al., 2016).

The formulations studied using the EDB instrument are presented in Table 1. For each case, two to five droplets were studied at a chamber temperature of 20 °C and relative humidity of ~0% or ~35%. This temperature was chosen based on the instrument limitations and also to allow accurate determination of the particle solidification behavior at higher temporal resolutions. The higher relative humidity was used to increase the relative temporal resolution of the EDB measurements in order to measure the onset of shell formation more accurately. The high total feed concentrations were chosen such that the shell formation would happen at large enough diameters to be accurately measured in the balance. The leucine concentrations were also chosen in such a way to cover a range of low saturation to high saturation.

Table 1 The composition of the samples studied using the electrodynamic balance, accompanied by their feed concentrations, measured average initial droplet diameters and the relative humidities studied for each case. The drying temperature was set to 20 °C for all cases. The tolerances of the initial droplet diameters are the standard deviation of multiple droplets studied for each case.

Sample Name	Total Solids Content (mg/mL)	Trehalose Mass Fraction (%)	Leucine Mass Fraction (%)	RH (%)	d_0 (μm)
EDB5L100	5	0	100	0, 35	53.0±1.6
EDB10L100	10	0	100	0, 35	53.4±0.2
EDB20L100	20	0	100	0, 34	53.0±0.2

EDB10T20L80	10	20	80	37	55.8±0.4
EDB10T50L50	10	50	50	37	53.4±0.1
EDB10T70L30	10	70	30	39	50.1±0.2
EDB10T80L20	10	80	20	34	52.8±0.0
EDB10T90L10	10	90	10	34	53.5±0.0
EDB10T100	10	100	0	38	53.4±0.2
EDB5T100	5	100	0	35	53.6±0.2

208

2.2.2. Monodisperse Droplet Chain Instrument

210 A custom-made droplet chain instrument was used to produce and collect monodisperse particles for

211 electron microscopy purposes (Baldelli et al., 2015; Baldelli and Vehring, 2016b; Ordoubadi et al., 2019).

212 In this setup, a droplet-on-demand piezoceramic dispenser with an orifice diameter of 40 µm (MJ-AL-

213 HT-40-8MX, MicroFab Technologies, Plano, Texas, USA) horizontally injected droplets into a vertical

214 glass tube with a frequency of 60 Hz. Dry air, at room temperature, passed through the flow tube from

215 above with a flow rate of approximately 10-15 L/min. Dried particles were then collected at the bottom of

216 the flow tube on a SEM sample stub with a hole drilled through it, onto which a membrane filter with a

217 pore size of 0.8 µm (Isopore Polycarbonate, Millipore, Darmstadt, Germany) was attached with the help

218 of a punched double-sided carbon tape. The other end of the SEM stub was connected to a vacuum line

219 with a monitored flow rate of about 10-15 L/min. The flow rate of the dry air passing through the flow

220 tube was slightly larger than the vacuum-line flow rate in order to maximize the collection efficiency of

221 the particles and reduce contamination from the surrounding environment. A lens and digital camera

222 system was used to measure the initial diameters of the generated droplets.

223 The formulations studied with this instrument are shown in Table 2. The formulations were chosen to be

224 similar to some of the formulations studied using the CK-EDB instrument. The average initial droplet

225 diameters were obtained using the image processing tool of MATLAB (MATLAB, 2019) from two sets

226 of images, one hundred per set, taken at the start and near the end of each experimental run to factor in

227 any changes in droplet diameter throughout the duration of the particle collection, which was about 3

228 hours.

Table 2 The composition of the samples studied using the droplet chain instrument, accompanied by their feed concentrations and measured average initial droplet diameters. The drying temperature was set to 20 °C for all cases. The tolerances of the initial droplet diameters are the standard deviation of hundreds of droplets per case.

Sample Name	Total Solids Content (mg/mL)	Trehalose Mass Fraction (%)	Leucine Mass Fraction (%)	d_0 (µm)
MDC5L100	5	0	100	39.8±0.1
MDC10L100	10	0	100	36.2±0.1
MDC20L100	20	0	100	35.8±0.4
MDC10T50L50	10	50	50	37.2±0.2
MDC10T80L20	10	80	20	37.1±0.3
MDC10T90L10	10	90	10	37.7±0.3
MDC10T100	10	100	0	42.4±0.1

2.2.3. Lab-scale Spray Drying

In order to produce enough powder for further characterization and also to assess the applicability of the conclusions obtained from the previous experiments in a manufacturing environment, a lab-scale spray dryer (B-191, Büchi Labortechnik AG, Flawil, Switzerland) was used in conjunction with a customized twin-fluid atomizer (Carrigy et al., 2019). A thermodynamic process model developed for this specific spray dryer was used to select process conditions so as to have appropriate outlet temperature and humidity, as explained elsewhere (Carrigy and Vehring, 2019). For all of the spray-dried formulations, the inlet temperature was set to 75 °C, the liquid feed flow rate was set to 2.5 mL/min, drying gas flow rate was 540 L/min, and atomizer air-to-liquid ratio was 10. Based on the process model, these parameters resulted in an outlet temperature of about 48 °C and predicted outlet relative humidity of about 7%. The measured outlet temperatures were between 48.6 and 49.2 °C. Based on the chosen air-to-liquid ratio and available characterization curve of the atomizer (Hoe et al., 2014), the initial mass median diameter of the atomized droplets was approximately 8 µm. The collected powders were stored in a dry box (RH ~ 0%) at room temperature (20 °C). The initial compositions of the spray-dried formulation are shown in Table 3. The formulations were chosen so that most of the resulting particles would be in the respirable regime. The leucine contents were also chosen to cover the probable transition from partially amorphous to fully crystalline state.

Table 3 The compositions, feed concentrations and approximate median initial droplet diameters of the spray-dried formulations. Inlet temperature was 75 °C for all cases.

Sample	Total Solids Content (mg/mL)	Trehalose Mass Fraction (%)	Leucine Mass Fraction (%)	$d_{0,50}$ (µm)
SD50T60L40	50	60	40	~8
SD50T80L20	50	80	20	~8
SD50T90L10	50	90	10	~8
SD50T100	50	100	0	~8

252

253 ## 2.3.　Characterization Techniques

254 ### 2.3.1.　Scanning Electron Microscopy

255 The micrographs presented in this article were obtained using a field emission scanning electron

256 microscope (Sigma FESEM, Zeiss, Jena, Germany) with an accelerating voltage of 5 kV and working

257 distances ranging from 5 to 10 mm.

258 The sizes of the particles obtained from the monodisperse droplet chain instrument were measured from

259 the SEM images at 1000× using ImageJ software (Schneider et al., 2012). The projected area of about 40

260 particles per sample was measured manually to find the average projected area diameter of the particles.

261 The projected area diameter represents the volume equivalent diameter of the particles only if the

262 particles are completely spherical. As will be seen later, for some of the studied cases the particles were

263 not completely spherical. Nevertheless, the projected area diameter was used as an estimate of the particle

264 sizes for each sample.

265

266 ### 2.3.2.　Raman Spectroscopy

267 Spray-dried powders were measured with a custom-designed dispersive Raman spectrometer (Wang et

268 al., 2017) to determine the solid phase of each component. Powder samples were first loaded into a 0.2 µl

269 cavity of an aluminum sample holder and kept under dry condition with less than 3% relative humidity

270 during spectra acquisition. A 671 nm diode laser (Ventus 671, Laser Quantum, UK) with a maximum

271 output power of 500 mW was used as the light source for Raman signal excitation. Raw trehalose and L-

272   leucine were measured directly as received to obtain their respective crystalline Raman reference spectra.

273   Spray-dried pure trehalose was measured to be amorphous and used as the reference spectrum (Feng et

274   al., 2011). Because an amorphous leucine powder reference could not be produced, the reference

275   spectrum of amorphous leucine was approximated by measuring its saturated aqueous solution and then

276   subtracting the spectrum of water. Characteristic peaks of the reference spectra for each component were

277   used to determine the solid phase of each component. A full multivariate deconvolution process, which

278   has been explained in detail elsewhere (Wang et al., 2017), was used to quantitatively determine the solid

279   phase of each component in multi-component systems. Briefly, spectral contributions of each component

280   were subtracted from the raw spectrum of the mixture until their respective characteristic peaks were

281   eliminated and a close-to-flat residual spectrum was obtained. The spectral intensities of each component

282   were then correlated to their corresponding mass fractions using a calibration factor obtained by

283   measuring a spray-dried powder with known mass fraction of amorphous leucine and using trehalose as

284   the internal reference.

285

286   ### 2.3.3. Time-of-Flight Secondary Ion Mass Spectrometry (TOF-SIMS)

287   The surface composition of the spray-dried powders was measured with an average depth of 3-5 nm

288   (Muramoto et al., 2012) using a TOF-SIMS instrument (TOF.SIMS[5], ION-TOF GmbH, Münster,

289   Germany) with Bi_3^+ ion source operating at 30 keV energy. Measurements were done on a raster size of

290   200 µm × 200 µm with a frame size of 1024×1024 pixels and five pulses per pixel. These frames were

291   then binned 2×2 for data processing, giving 512×512 pixels. The spectrum of each raw material was also

292   measured as a reference spectrum. The composition of each pixel was obtained from fitting the spectrum

293   at that pixel to a linear combination of reference spectra obtained by a non-negativity constrained

294   alternating least squares method. Further details on the processing of the SIMS spectra can be found in

295   another publication by the authors (Nicholas et al., 2020).

296   To represent the average surface compositions, for each sample, a single 512×512 pixel 16-bit RGB

297   image was then obtained from the spectra matrices, with the red channel reserved for leucine, the blue

298   channel reserved for trehalose and the green channel not used. Image analysis was performed using

299   MATLAB to obtain the average surface composition of each material for the whole frame and the surface

300   compositions of different size fractions of particles, i.e. small (less than 1 µm diameter), medium

301   (between 1 and 3 µm diameter) and large (greater than 3 µm diameter). The color intensity (0-255 for 16-

302   bit channels) of each pixel was read and used to find the surface compositions. If the total intensity of a

303   pixel was less than 1, that pixel was not used in the statistical calculations further on, in order not to

304   account for pixels that were not part of any particle. The average of all the acceptable pixels of each

305   image was then used to find the average surface coverage of each component for the whole frame and for

306   each of the size ranges. Grouping of particles based on their sizes was performed as follows. Around 30

307   particles per size-bin per sample were randomly selected from each frame and manually moved onto an

308   empty black frame using imageJ software. These mostly black images were then used to find the surface

309   composition of each size range. The molar-based surface compositions were in turn converted into mass

310   fractions to compare with the bulk fractions of the formulations studied.

311

312   2.4.   Particle Formation Theory

313   A preliminary understanding of the different phenomena occurring during droplet evaporation and the

314   eventual solids formation and crystallization, requires some knowledge of the basics of particle formation

315   theory. Predictions based on such theory can help a formulator in early design stages. The most

316   straightforward relationship used to predict the final particle sizes during spray drying is based on a

317   simple mass balance as (Vehring, 2008)

$$d_{\mathrm{p}} = \sqrt[3]{\frac{C_{0,\mathrm{t}}}{\rho_{\mathrm{p}}}}\, d_0, \tag{1}$$

318   in which, d_p is the volume equivalent particle diameter, $C_{0,t}$ is the initial total solids concentration, ρ_p is

319   the particle density and d_0 is the initial droplet diameter. The use of equation (1) requires the particle

320   density to be known in advance, which is typically not the case for rugose and hollow particles. Particle

321   density is defined as the total mass of the dried particle divided by the particle volume including the

322   internal and external voids. For solid and spherical particles, such as spray-dried trehalose, the particle

323   density can be assumed to be equal to the material's true density, e.g. 1530 mg/mL for amorphous

324   trehalose (Vehring et al., 2007). If the particle density is not known, a value of 1000 mg/mL can be

325   considered as a rough approximation. Based on the inverse cube root relationship, the effect of particle

326   density on the particle diameter is relatively small.

327   There is a linear correspondence between the particle and initial droplet diameters, which makes the

328   particle diameter more sensitive to the atomized droplet size distribution. For polydisperse spray drying

329   applications, the mass median diameter (MMD) of the atomized droplets is usually used as d_0 in equation

330   (1) to give the mass median diameter of the spray-dried powder.

331   The presence of dispersibility enhancers such as leucine and trileucine in the formulation results in the

332   production of rugose and thin-shelled particles, for which, as will be seen later, particle densities of as low

333   as 300 mg/mL can be achieved. In these cases, a more advanced understanding of the internal

334   distribution, precipitation, and phase separation behavior of each component is required for successful

335   particle design.

336   In an evaporating solution droplet, the recession of the liquid/air interface causes surface enrichment by

337   the solutes. This means that the concentration of the solutes on the surface will be higher than at the

338   center of the droplet. This induced concentration gradient causes a radial diffusion flux of each species

339   from the surface towards the center (Boraey and Vehring, 2014; Vehring et al., 2007). The larger or less

340   mobile the solute molecules are, the smaller their diffusional flux will be, which means a higher level of

341   surface enrichment. For example, a polymer with a large molecular size causes early shell formation

342   during drying (Carrigy et al., 2019). The magnitude of surface enrichment during droplet evaporation can

15

343   be calculated by solving the mass transfer equation inside the droplet (Boraey and Vehring, 2014;

344   Ordoubadi et al., 2019; Vehring et al., 2007). The surface enrichment is defined mathematically as the

345   instantaneous surface concentration of each solute normalized by the mean concentration of that solute

346   inside the droplet. This normalized parameter has an asymptotic behavior and over time approaches a

347   value called the steady-state surface enrichment, $E_{s,i}$. For small molecules, this steady-state value can be

348   obtained from what is known as the VFL method (Vehring et al., 2007):

$$E_{s,i} = \frac{C_{s,i}}{C_{m,i}} \approx 1 + \frac{Pe_i}{5} + \frac{Pe_i^2}{100} - \frac{Pe_i^3}{4000} \qquad Pe_i = \frac{\kappa}{8D_i} < 20, \qquad (2)$$

349   where $C_{s,i}$ and $C_{m,i}$ are the instantaneous surface and mean concentrations, respectively and Pe_i is the

350   Péclet number of the ith component. Here, κ is the evaporation rate of the droplet (defined later) and D_i is

351   the mass diffusion coefficient of the respective component. The Péclet number compares the timescales

352   associated with surface recession and diffusion. A very large Péclet number ($Pe > 20$) means the solute

353   does not have enough time to diffuse inwards due to the rapid recession of the droplet surface. This

354   phenomenon results in a very high surface enrichment and large concentration gradients near the surface,

355   but relatively constant concentrations elsewhere. At these high Péclet numbers, the steady state surface

356   enrichment is only reached at the very end of the droplet evaporation time. At moderate Péclet numbers

357   ($0.5 < Pe < 20$), the intensities of diffusion and surface recession are relatively equal, and there will be a

358   smooth concentration profile with a maximum at the surface and a minimum at the droplet center. For low

359   Péclet numbers ($Pe < 0.5$) the evaporation rate is much smaller than the diffusion of the solute such that

360   the internal concentration will be approximately equal to the mean concentration at each time throughout

361   the droplet. In this case, the steady state surface enrichment is approached quite early, and it can be

362   assumed that the surface enrichment is equal to the steady state value obtained from equation (2). The

363   evaporation rate is defined as

$$\kappa = -\frac{\mathrm{d}d^2}{\mathrm{d}t}, \qquad (3)$$

364   in which d is the instantaneous diameter of the droplet. The evaporation rate is constant for a large

365   proportion of the droplet drying time for single-solvent formulations and can be obtained from the

366   solution of the coupled heat and vapor mass transfer equations around a spherical droplet (Gregson et al.,

367   2019; Ordoubadi et al., 2019). Using a numerical model (Ordoubadi et al., 2019), the evaporation rates of

368   water droplets at different drying temperatures and four different relative humidities were calculated and

369   are shown in Figure 1. The evaporation rates at higher relative humidity values are presented as a

370   reference for comparison, because in actual spray dryers the humidity can be high in the vicinity of the

371   spray plume due to high spray rates and low temperatures due to evaporative cooling. It is worthwhile to

372   note that at higher relative humidity values, droplets begin to boil at lower drying temperatures, at which

373   the evaporating droplet temperature approaches 100 °C, represented by the gray dashed line and arrow in

374   this figure, after which no increase in evaporation rate is possible.
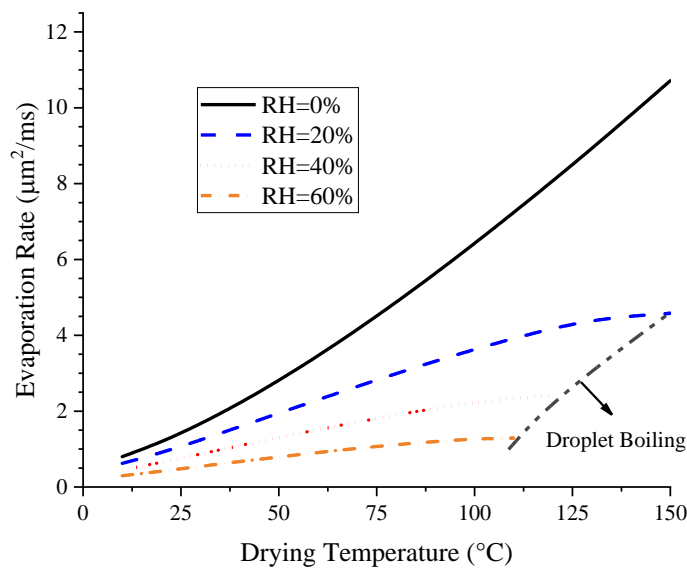
375

376   **Figure 1** Water droplet evaporation rates, κ, at different drying temperatures and relative humidities.

377   Using a simple mass balance between the initial droplet state and any time during the drying period, the

378   mean concentration of any solute in solution form can be obtained from (Vehring, 2008):

17

$$C_{m,i}(t) = C_{0,i}\left(1 - \frac{t}{t_d}\right)^{-\frac{2}{3}},\tag{4}$$

379   in which $C_{0,i}$ is the initial feed concentration of the solute and t_d is the droplet lifetime. Equation (4) can

380   be obtained by assuming a constant evaporation rate and integrating equation (3) to give $d^2(t) = d_0^2 -$

381   κt, and then using this result for the diameter in the mass balance equation. The droplet lifetime can be

382   obtained similarly by setting the diameter equal to zero, which gives

$$t_d = \frac{d_0^2}{\kappa}.\tag{5}$$

383   In a simple particle formation model, for a crystallizing component such as leucine, the time at which

384   saturation is reached (e.g. $C_{s,leu} = C_{sol,leu} = 22$ mg/mL) is usually considered as a first instance at which

385   nucleation can commence. By using equation (4) and the definition of surface enrichment, it is possible to

386   obtain the time needed by any component to reach saturation from

$$t_{sat,i} = t_d\left[1 - \left(S_{0,i}E_{s,i}\right)^{\frac{2}{3}}\right],\tag{6}$$

387   where $S_{0,i}$ is the initial concentration of the solute normalized by its solubility, i.e. the initial saturation

388   ratio of the solute. Note that it is assumed that the surface enrichment is approximately equal to the steady

389   state surface enrichment, $E_{s,i}$, during much of the droplet lifetime, which is true for small Péclet numbers

390   associated with small molecules, such as trehalose and leucine. For larger Péclet numbers, the

391   relationships presented in (Boraey and Vehring, 2014) can be used to find the instantaneous surface

392   enrichment.

393   Upon reaching supersaturation, some time is required for the solute molecules to crystallize before the

394   remaining water content of the droplet is evaporated off and the molecules lose their mobility. Another

395   important timescale that determines the crystallization behavior of a component is the available time for

396   crystallization or the precipitation window, defined as

$$t_{p,i} = t_d - t_{sat,i} = t_d \left(S_{0,i} E_{s,i}\right)^{\frac{2}{3}}, \tag{7}$$

397   or in dimensionless form as

$$\tau_{p,i} = \frac{t_{p,i}}{t_d} = \left(S_{0,i} E_{s,i}\right)^{\frac{2}{3}}. \tag{8}$$
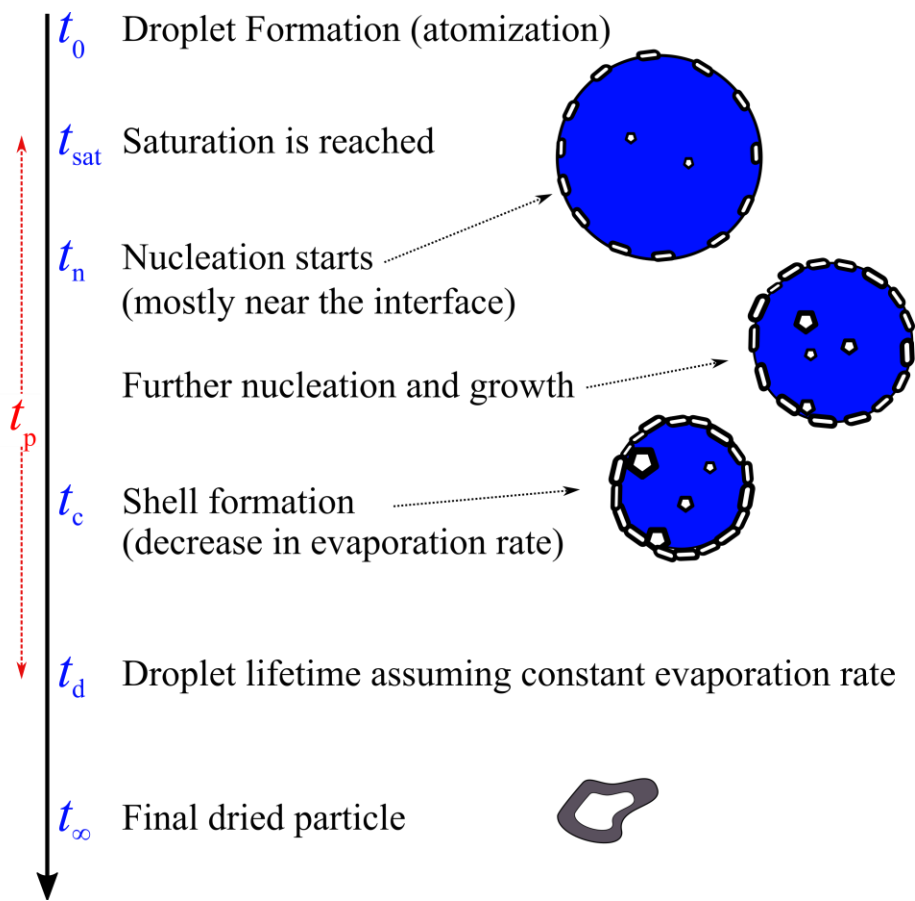
398   In the remainder of this article, the Greek letter τ will denote the dimensionless time of the respective

399   timescale normalized by the droplet drying time. The larger this value, the more crystallinity is expected

400   for a crystallizing component (Feng et al., 2011). The presence of another component such as a saccharide

401   (e.g. trehalose) can also hinder the mobility of the crystallizing components due to the increase in

402   viscosity of the solution at higher saccharide concentrations (Galmarini et al., 2011) or their earlier

403   solidification. This explains the fact that leucine has a higher amorphous fraction in spray-dried powder

404   with high fractions of trehalose (Feng et al., 2011).

405   For nucleation to start and stable nuclei to form and grow, a certain level of supersaturation is required to

406   surpass the energy barrier of nucleation (Mullin, 2001). Therefore, a more relevant point during the

407   evaporation history can be identified, namely the critical supersaturation ratio, $S_{n,i}$ at which the

408   component can instantaneously nucleate. In a manner similar to the derivation of equation (6), the time to

409   reach this critical supersaturation, $t_{n,i}$, can be obtained as

$$t_{n,i} = t_d \left[1 - \left(\frac{S_{0,i} E_{s,i}}{S_{n,i}} \right)^{\frac{2}{3}} \right]. \tag{9}$$

410   Upon reaching this level of supersaturation, nucleation can start on the surface of the droplet. The

411   subsequent growth of the crystallites reduces their mobility and causes their Péclet numbers to increase

412   substantially, meaning that any crystallite that is collected by the receding surface of the droplet is

413   practically trapped on the surface. Further surface accumulation of these crystallites and their

414   simultaneous growth causes a solid shell to form on the surface of the droplet (Baldelli et al., 2016) at

415   time t_c, defined as the time of shell formation. Upon reaching this time, the evaporation rate as defined by

416　equation (3) is reduced substantially, even though the particle continues to lose water and may shrink

417　further. This process, as shown schematically in Figure 2, explains the observed hollow particle

418　morphologies for a crystallizing material with low aqueous solubility such as leucine, (Feng et al., 2011;

419　Vehring, 2008). For a component that crystallizes during drying, the time of shell formation, t_c, does not

420　follow the behavior of the other timescales such as t_n, t_{sat} and t_d. This is because the rates of nucleation,

421　crystal growth and surface accumulation cannot be correlated with the evaporation rate alone. For this

422　reason, it is possible instead to find t_c from the EDB observations, defined in this article as the time at

423　which deviation from d^2-law is observed in the evaporation history, rather than by using the mass balance

424　equations similar to equation (6).

t_0　Droplet Formation (atomization)

t_{sat}　Saturation is reached

t_n　Nucleation starts
(mostly near the interface)

Further nucleation and growth

t_p

t_c　Shell formation
(decrease in evaporation rate)

t_d　Droplet lifetime assuming constant evaporation rate

t_∞　Final dried particle

425

426　**Figure 2** The proposed particle formation process and characteristic times for a crystallizing component

427　with low solubility.

428   He et al. successfully measured the critical supersaturation at which nucleation commences

429   instantaneously in evaporating microdroplets via the extrapolation of nucleation times for a broad range

430   of compounds and proposed a practical model to predict this critical supersaturation, S_n, based on

431   classical nucleation theory and as a function of crystal and solution properties (He et al., 2006). The

432   appropriate properties for leucine in aqueous solutions were crystalline leucine density, $\rho_{leu} = 1293$

433   mg/mL (Yaws, 2010) and its aqueous solubility, $C_{sol,leu} = 22$ mg/ml at 25 °C (Yalkowsky et al., 2019).

434   The activity coefficient of water at leucine saturation was approximated to be equal to 1 (Held et al.,

435   2011). Inserting these values in equations given by He et al. gave $S_{n,leu} = 3.5$. Hence, based on this

436   simple model, leucine was expected to start nucleating instantaneously at a supersaturation of 3.5 in a

437   water microdroplet.

438   For materials that are spray dried into an amorphous state, such as trehalose (Feng et al., 2011) and

439   pullulan (Carrigy et al., 2019), solidification starts upon reaching a very high concentration, denoted as

440    $C_{c,i}$ in this study. The time to reach this critical concentration can be obtained from

$$\tau_{c,i} = 1 - \left(\frac{C_{0,i}E_{s,i}}{C_{c,i}}\right)^{\frac{2}{3}}. \tag{10}$$

441   Note that based on the Stokes-Einstein equation, the diffusion coefficients of leucine and trehalose in

442   water at 20 °C are 6.6×10^{-10} and 5.2×10^{-10} m²/s, respectively. These give Péclet numbers of about

443   0.8 and 1.1 at a drying temperature of 75 °C and 0.2 and 0.3 at a drying temperature 20 °C, for leucine

444   and trehalose, respectively. Hence, for the drying temperatures encountered in this study, the use of the

445   steady state surface enrichment equations is reasonable. If that is not the case for a large excipient or API

446   or at much higher evaporation rates, the methodology presented in (Boraey and Vehring, 2014) can be

447   employed to approximate the evolution of surface enrichment with time.

448   The important time scales and diameters encountered in this study are summarized in Table 4.

Table 4 Important time scales and diameters relevant to the solidification and shell formation of the particles encountered in this study.

Parameter	Dimensionless Form	Description
t_d	-	The drying time of the droplet assuming constant evaporation rate (equation 5).
$t_\text{n,leu}$	$\tau_\text{n,leu} = t_\text{n,leu}/t_\text{d}$	The time for leucine to reach its critical supersaturation. Obtained from equation 9 with $S_\text{n,leu} = 3.5$.
t_c	$\tau_\text{c} = t_\text{c}/t_\text{d}$	The time of shell formation or solidification obtained from the EDB measurements.
$t_\text{c,leu}$	$\tau_\text{c,leu} = t_\text{c,leu}/t_\text{d}$	The time of shell formation of leucine obtained from equation 11, which was a non-linear fit based on the EDB measurements.
$t_\text{c,treh}$	$\tau_\text{c,treh} = t_\text{c,treh}/t_\text{d}$	The solidification time of trehalose obtained from equation 10 with $C_\text{c,treh} = 830$ mg/mL. This concentration was obtained from the EDB measurements.
d_0	-	The initial droplet diameter.
d_c	d_c/d_0	The diameter at which shell formation or solidification was detected in the EDB measurements.
d_p	d_p/d_0	The final projected area equivalent diameter of the monodisperse particles generated using the droplet chain instrument.

451

452

3. Results and Discussions

As mentioned in the previous sections, different combinations of trehalose and leucine were studied. The main object of the experimental procedure was to study the shell formation and crystallization kinetics of leucine-containing particles to support future mechanistic design attempts in spray drying microparticles containing different excipients and APIs intended for pulmonary aerosol delivery.

3.1. Comparative-Kinetics Electrodynamic Balance

The CK-EDB instrument allowed the accurate measurement of the time at which deviation from d^2-law is observed in the evaporation history, which we define here as the time to shell formation t_c. A novel method was also employed to approximate the general morphology of the solution droplet based on the irregularities observed in the phase function of the scattered light (Haddrell et al., 2019). Two to five droplets per formulation (Table 1) were studied at 20 °C and at dry (RH = 0%) and humid (RH ≈ 35%) conditions. Samples of droplet data per formulation are shown in Figure 3. The data points are color-coded based on the detected morphologies. The square of the droplet diameter is plotted as a function of time, yielding a straight line for constant-rate evaporation according to the d^2-law. However, the droplet diameters are only reliable for the completely spherical morphologies (color-coded dark blue). It can be seen that there is some noise in most cases during the initial or middle stages of the evaporation upon droplet generation, resulting in unexpected morphology results like a core-shell structure early in the evaporation process (color-coded red). These anomalies may have been be caused by instability of the droplet inside the chamber.

By reviewing the droplet data for pure leucine cases in Figure 3, i.e. the first row of panels, a region can be observed at which inclusions were detected, shown by the black points. At these instances, significant deviation from the d^2-law, i.e. from a constant evaporation rate, is also visible. Later on, the morphology was detected to be non-spherical or non-homogenous, denoted by the purple points. Increasing the initial concentration of leucine accelerated the occurrence of this critical point, meaning that the inclusions happened at a larger droplet diameter. It was also observed that increasing the initial leucine concentration likewise caused the elapsed time between the onset of inclusions and the first non-spherical point (purple points) to increase.

These observations agree with our previous explanation regarding leucine particle formation (Figure 2). A critical supersaturation is reached at the time ($t_{n,leu}$) at which nucleation commences. This point cannot be detected in the measurements because the droplet is still optically homogeneous with nuclei present

23

483   that are too small to be detected by changes in the phase function. Then the crystallites grow and enrich

484   the surface to a point at which the phase function of the scattered light is affected, and the evaporation

485   rate is decreased. At this point the time for shell formation ($t_{c,\text{leu}}$) is reached. The detected morphologies

486   in Figure 3 follow the same sequence, showing optically homogeneous spheres during the constant rate

487   evaporation phase, inclusions and core-shell structures at the point of shell formation and then non-

488   spherical, irregular morphology once the shell begins to deform or fold.

489   In the cases of mixtures of leucine and trehalose, shown in the next five plots in Figure 3, similar behavior

490   was observed. Increasing the leucine fraction at constant total solids content initiated shell formation at an

491   earlier time, indicating the potential to obtain larger, less dense and more rugose particles. By a

492   qualitative comparison of plots for the samples EDB5L100 (5 mg/mL pure leucine) and EDB10T50L50

493   (10 mg/mL with 50% leucine), which had the same absolute initial leucine concentrations, relatively

494   similar behavior was observed. The shell formation time was also similar. From this observation, we can

495   conclude that at high leucine fractions, trehalose does not interfere with the crystallization of leucine. For

496   the cases with leucine fractions less than 30%, a reversal in behavior was observed. No significant period

497   of inclusions and crystal growth was observed before complete solidification. For the case of 10%

498   leucine, the particles remained spherical even after the evaporation rate was reduced. These observations

499   are in agreement with previous studies which demonstrated that high fractions of trehalose can hinder the

500   crystallization of leucine to the point at which leucine is mostly amorphous, possibly due to rapid increase

501   of droplet viscosity (Feng et al., 2011).
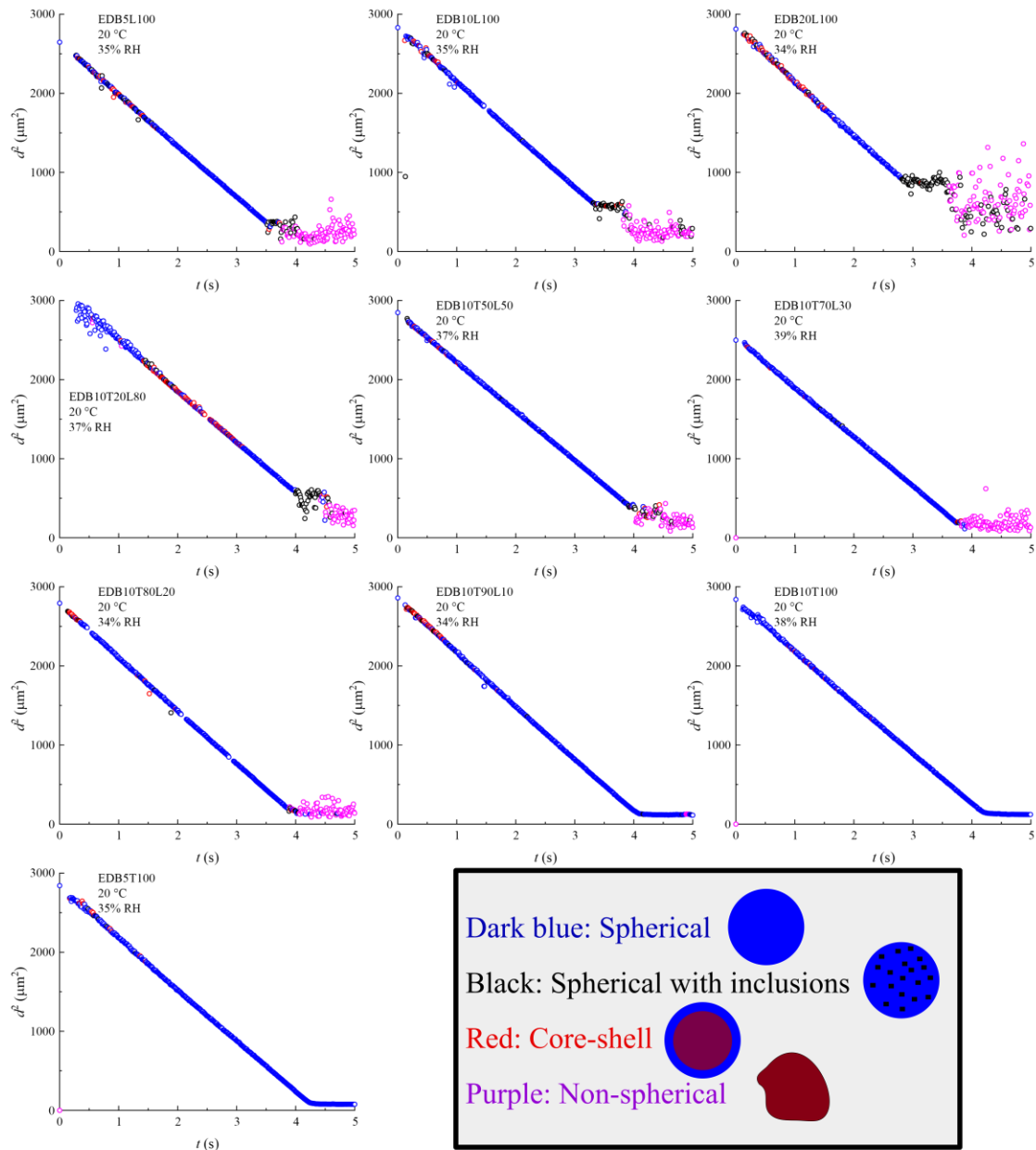
Figure 3 Sample droplet evaporation histories of the formulations studied using the CK-EDB instrument. The data are color-coded according to the detected morphologies. A label such as EDBαTβLγ means the formulation studied with the EDB instrument had a total feed concentration of α with trehalose and leucine mass fractions of β and γ, respectively.

507   For the last two formulations of neat trehalose, a very sharp drop in the evaporation rate was observed

508   after which a spherical particle was detected. This was expected, as neat spray-dried trehalose particles

509   are spherical (see Figure 7). Using the measured diameter at the points at which the evaporation rates

510   decrease, a trehalose bulk concentration at which solidification commenced was obtained. The measured

511   concentration was practically the same for the two cases studied, each with a number of replicates. We

512   call this concentration the solidification concentration for trehalose, $C_{c,treh} = 830 \pm 15$ mg/mL; the error

513   represents one standard deviation. It was shown previously that the particle density of spray-dried

514   trehalose particles was approximately equal to the density of amorphous trehalose, which is 1530 mg/mL

515   (Vehring et al., 2007). The lower measured critical concentration for trehalose points to the fact that the

516   particles keep shrinking at a much smaller rate, while losing their water content, until the true density is

517   reached.

518   For all of the experiments performed (2-5 droplets per formulation), the shell formation time, t_c, and

519   corresponding diameter, d_c, were measured. The normalized values $\frac{d_c}{d_0}$ and $\tau_c = \frac{t_c}{t_d}$ are plotted as a

520   function of initial leucine concentration in figures 4 and 5, respectively. In these figures, the error bars

521   represent one standard deviation. As seen from these plots and as pointed out earlier, the time of shell

522   formation was decreased, and the critical diameter increased, by increasing the initial leucine

523   concentration. These phenomena can be explained by the fact that leucine reaches critical supersaturation

524   earlier in the evaporation process if the initial leucine concentration is higher (see equation (9)). This

525   trend was similar between the pure leucine formulations and the formulations containing trehalose. Again,

526   this fact points to our previous observation that trehalose has no discernible effect on the crystallization

527   and shell formation of leucine at high leucine fractions. The mean concentrations of leucine at the point of

528   shell formation, $C_{c,leu}$, were also calculated from a mass balance equation and are shown in Figure 6. The

529   level of leucine saturation is also shown on the right axis. The leucine concentration at the point of shell

530   formation was 5±1 and independent of the initial leucine concentration. For leucine solution droplets with

531   an initial diameter of about 50 µm, shell formation can be detected at a supersaturation of about 5, which,

532   as expected, is larger than the previously calculated critical supersaturation of 3.5, because nucleation and

533   some crystal growth must precede the point of shell formation. Therefore, the time of shell formation and

534   its related normalized parameters, $\frac{d_c}{d_0}$ and τ_c, are suspected to be also a function of initial droplet diameter.

535   These assumptions will be verified by comparing the morphologies of polydisperse spray-dried particles

536   of different sizes of the same formulation later on. A detailed analysis of the combination of these effects

537   is outside the scope of this study.

538   Interestingly, it was noticed that the points in Figure 5 can be fitted using a function such that $\tau_{c,leu} =$

539    $1 - a\left(C_{0,leu}\right)^{2/3}$, where a is the fitting parameter. According to the explanation above, a is expected to be

540   a function of the initial droplet diameter and possibly the evaporation rate for smaller droplets. Comparing

541   this function to equations obtained from mass balance, such as equations (6) and (9), a non-linear fit was

542   performed on the data to find the diameter dependent coefficient k_{d0} such that

$$\tau_{c,leu} = 1 - k_{d0}\left(E_{s,leu}S_{0,leu}\right)^{2/3}, \tag{11}$$

543   which resulted in $k_{d0} = 0.35$ for the parameters of the CK-EDB experiments with initial diameters of

544   about 50 µm. Like a, this coefficient should also be a function of other process parameters such as the

545   evaporation rate. The sensitivity of this coefficient to other parameters is believed to be lower than it is to

546   the droplet diameter, as it was observed that τ_c was practically constant for different droplets studied for a

547   single formulation but at two different relative humidities (hence different evaporation rates). Using this

548   empirical equation, one can predict the instance of shell formation for leucine in the course of droplet

549   evaporation. This time-point can be compared to the critical points of other components in the system in

550   order to predict the levels of surface coverage. The dimensionless time to reach critical supersaturation,

551   τ_n, obtained from equation (9), can also be compared to the time of shell formation of other components

552   to check if leucine has enough time to nucleate in the first place. Previously, the time to reach saturation

553   was used for this purpose (Vehring, 2008), but the theoretical time to critical supersaturation and the time

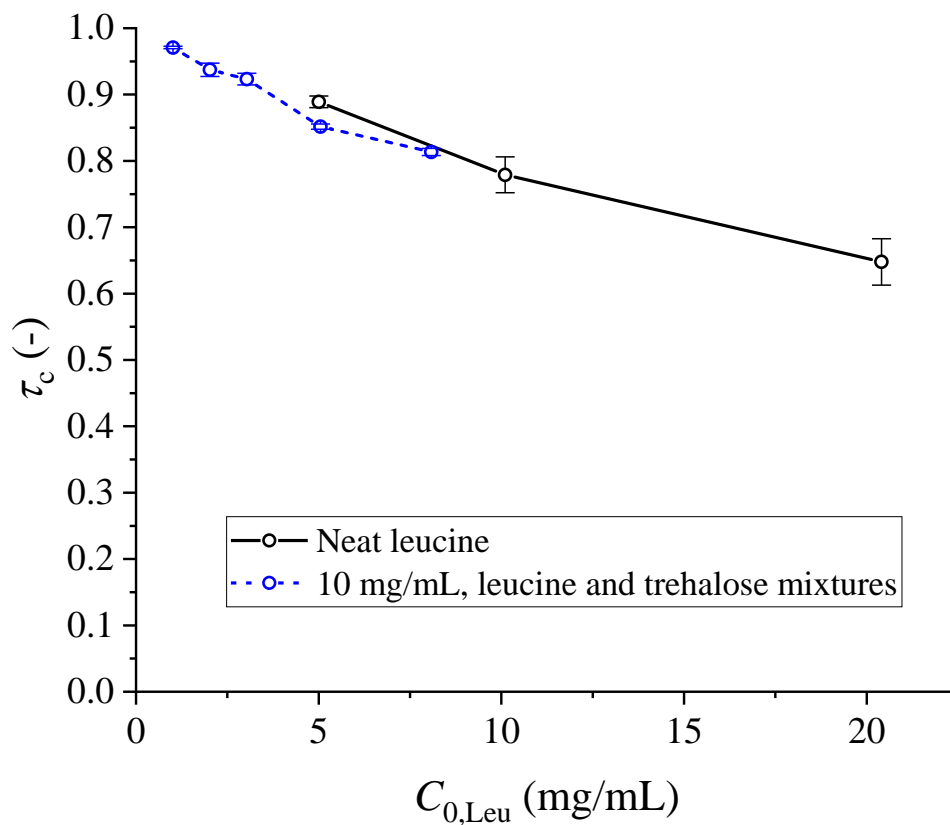554   of shell formation are better approximations for the actual shell formation timing.

555
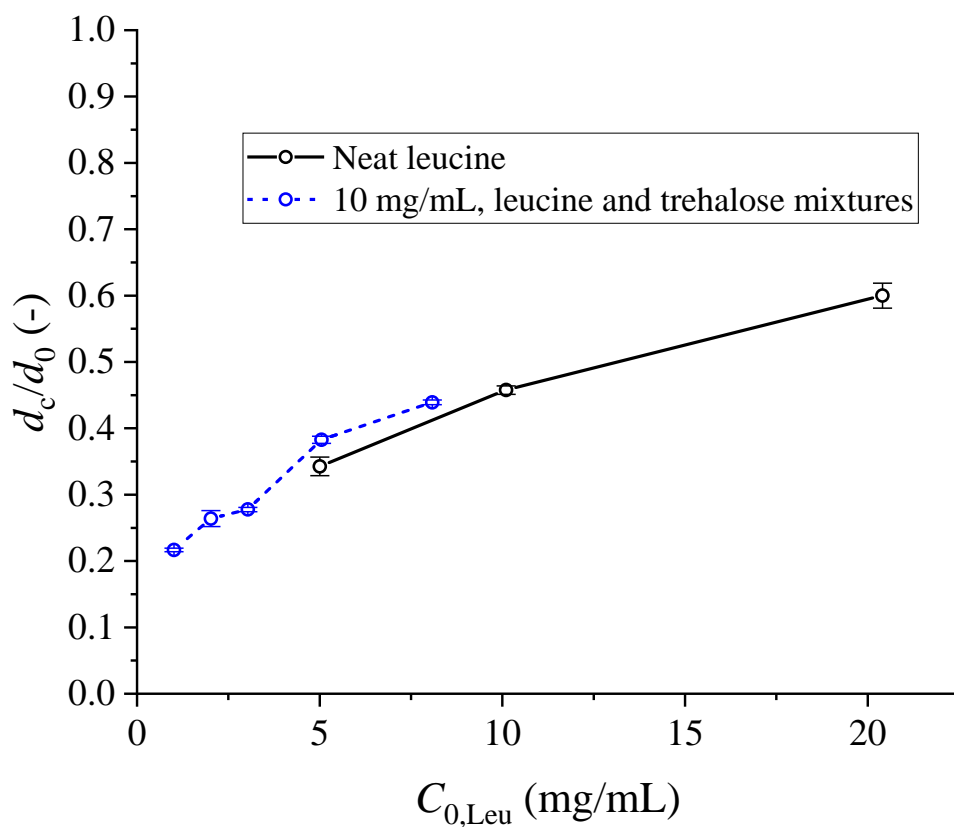
Figure 4 The normalized diameter of shell formation obtained from CK-EDB measurements, for $d_0 \cong$

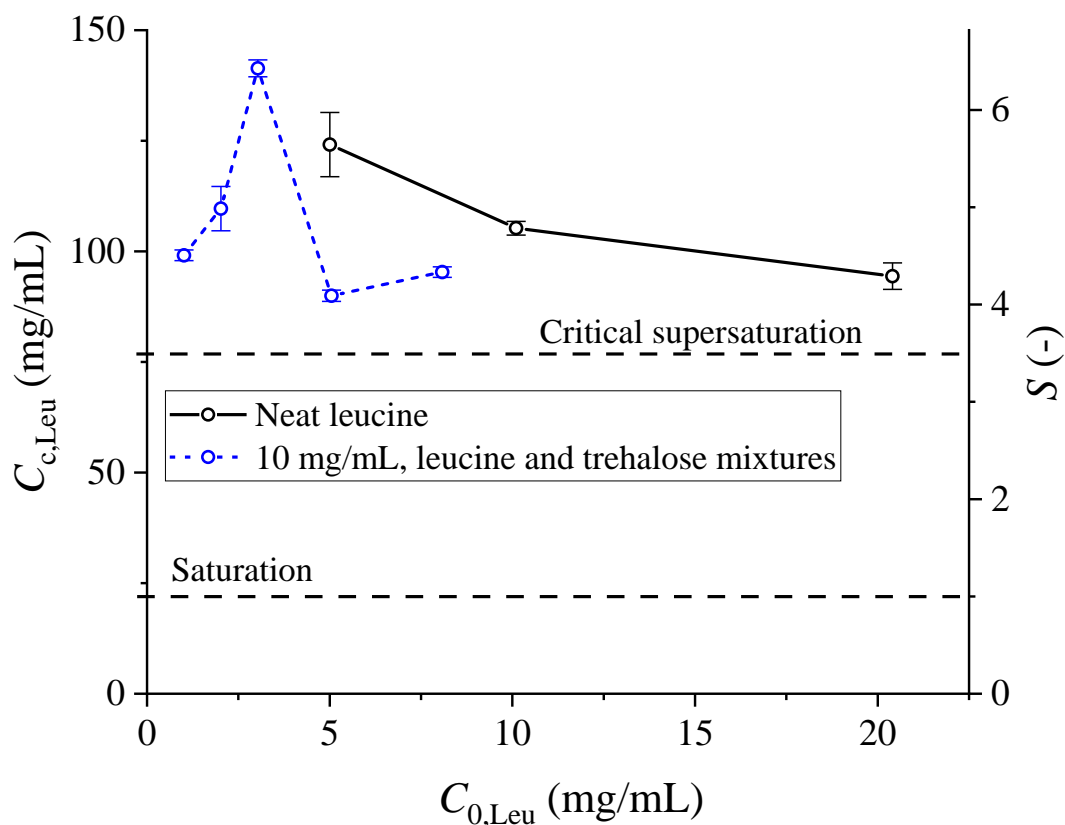557   50 μm.

558

Figure 5 Normalized time of shell formation obtained from CK-EDB measurements, for $d_0 \cong 50$ μm. The normalization was performed using the droplet drying time. Larger values mean shell formation happens later and closer to the end of the evaporation period.

559

560

561

562

563

Figure 6 The mean leucine concentration and saturation ratios at the point of shell formation, obtained from the CK-EDB measurements, for $d_0 \cong 50$ µm. The dashed horizontal lines represent the saturation at the leucine solubility concentration of 22 mg/mL and the theoretical critical supersaturation ratio of 3.5.

3.2. Monodisperse Droplet Chain Instrument

In order to measure the particle densities and show the corresponding particle morphologies of the cases studied using the CK-EDB instrument, similar formulations were analyzed using the droplet chain instrument (see Table 2). The SEM micrographs of these particles are shown in Figure 7. The first three micrographs for the neat-leucine cases show a morphology consistent with previously published results (Feng et al., 2011), namely a hollow core with a shell that consists of smaller individual pieces. Increasing

575   the initial concentrations resulted in larger particles with thicker shells. This result is expected, as higher

576   initial leucine concentrations mean critical supersaturation and the time of shell formation are reached

577   earlier and at larger droplet diameters. It is apparent from the last four micrographs that decreasing the

578   leucine content in a leucine/trehalose mixture causes the morphologies of the particles to change from

579   hollow ones with shells to solid spheres. As will be seen for the spray-dried particles, and as was also

580   shown elsewhere (Feng et al., 2011), decreasing the leucine content also decreases its crystalline fraction.

581   The ultrahigh magnification inset figures were included to show the patched surfaces due to presence of

582   crystalline leucine compared to the relatively smooth surfaces of amorphous trehalose particles.

583   As explained previously, the projected area diameter of these particles was measured as a representation

584   of their size. The resulting particle diameters, d_p, normalized by the measured initial diameters, d_0, are

585   presented in Figure 8. Because of the high accuracy in the measurement of the initial droplet diameters

586   and the high monodispersity of the particles, the particle densities could be obtained confidently using

587   equation (1). The measured particle densities are also shown in blue (right axis) in Figure 8. In this figure,

588   error bars represent one standard deviation. As expected, increasing the initial leucine concentration

589   caused the normalized particle diameters to increase, and the particle densities to decrease. It was

590   observed that at a leucine fraction of 50% the particle density was reduced by more than 60%. It was also

591   observed from the two cases at 5 mg/ml leucine, MDC10T50L50 and MDC5L100, that the general

592   morphology of the particles was similar. This fact points to previous observations that at mass fractions of

593   up to around 80% trehalose does not interfere with the crystallization and shell formation of leucine (Feng

594   et al., 2011). It is also worthwhile noting that the general trend and the actual values in this figure are very

595   similar to the data in Figure 4. These similarities may be due to the slow drying kinetics in the droplet

596   chain and the CK-EDB instruments as well as to the relatively large initial droplet diameters in both

597   instruments. Hence, enough time for crystal growth is available in both experimental techniques. Under

598   these circumstances the lowest particle densities can be achieved by choosing an initial leucine

599   concentration close to its solubility of 22 mg/mL at room temperature.

31

600
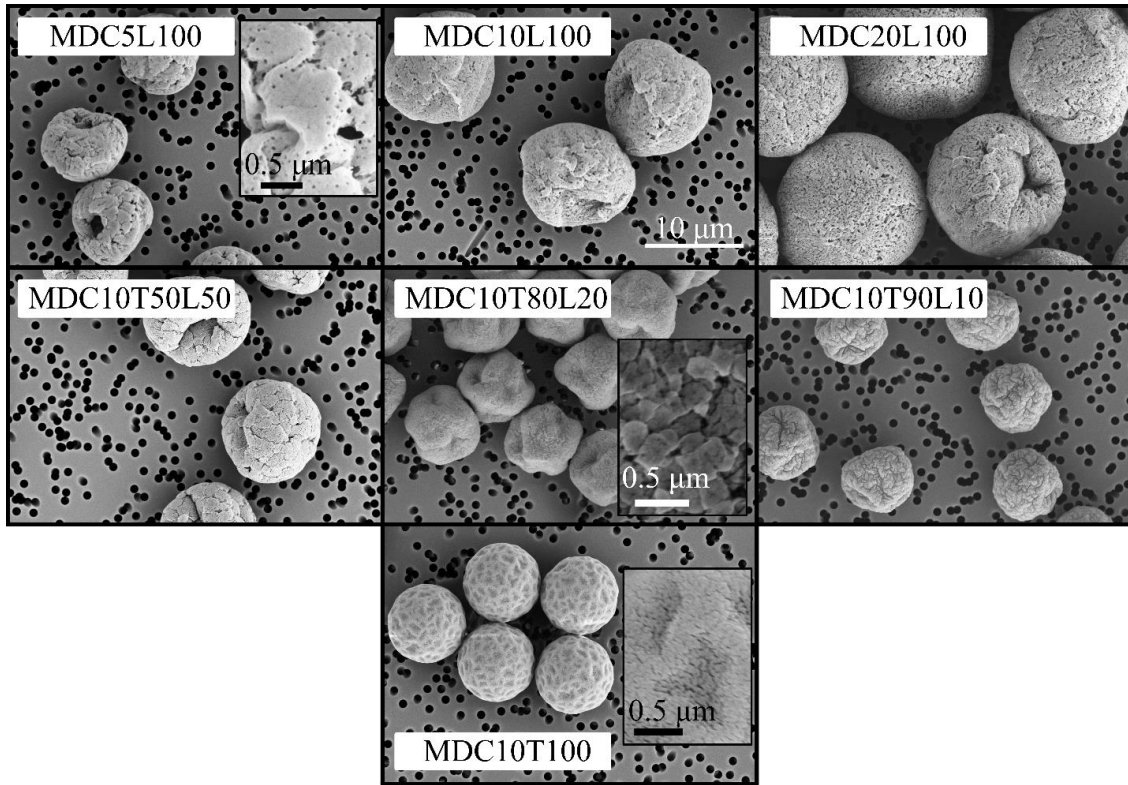
Figure 7 SEM micrographs of the particles generated using the monodisperse droplet chain setup at 20

°C with initial droplet diameters of about 40 µm. The 10-µm scale bar applies to all images except the

inset figures, for which separate scale bars are provided. A label such as MDCαTβLγ means the

formulation studied with the MDC instrument had a total feed concentration of α with trehalose and

leucine mass fractions of β and γ, respectively.
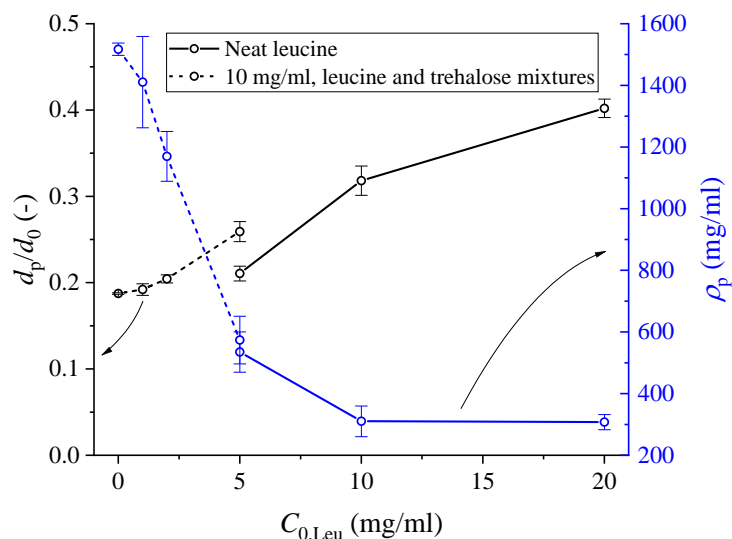
Figure 8 The measured normalized particle diameters and densities obtained from the monodisperse droplet chain setup at 20 °C with initial droplet diameters of about 40 µm.

3.3.   Spray-Dried Powder

The SEM micrographs of the four different spray-dried formulations containing leucine and trehalose are shown in Figure 9. The increase in surface roughness due to the shell formation and crystallization of leucine is clear, which is an important factor for the reported enhancement of aerosolization properties of such powders (Eedara et al., 2018; Mah et al., 2019; Seville et al., 2007). Similar to the monodisperse particles obtained from the droplet chain, surfaces of the particles for which leucine is expected to be crystalline were composed of distinguishable crystals, as seen from the higher-magnified micrographs at the bottom row of Figure 9.

Another important note to take from these images of the polydisperse powder is the difference in morphologies observed for a single formulation. Larger particles were hollow with a thinner shell, while smaller particles were denser. This difference supports our previous remarks that the whole process of crystallization and shell formation cannot be normalized by the drying time as can be done for amorphous

622   precipitation, e.g. for trehalose particles. This fact is also expected to cause variations in surface

623   compositions of the particles, with larger particles having higher leucine surface fractions, as will be seen

624   from the TOF-SIMS data below.

625   The leucine crystalline fractions obtained from the deconvolution of the Raman spectra are presented in

626   Figure 10, accompanied by the results of Feng et al. (Feng et al., 2011). Note that the total concentrations

627   were different compared to the formulations studied in the present article, hence the differences between

628   the data. Feng et al. mentioned that the formulation with 5% leucine fraction was dominantly amorphous,

629   but quantification was not possible due to the very small amount of leucine in the particle. The trehalose

630   was completely amorphous in all cases, as expected. In the current study, there was a transition from

631   partially to completely crystalline leucine between leucine fractions of about 10% to 20%. A mixture of

632   amorphous and crystalline molecules of the same material in the particles is undesirable for long-term

633   stability. That is because, in humid conditions, the crystals in the particles can act as nucleation sites for

634   the crystallization of the amorphous content of the same material. In other words, the crystalline content

635   of a material lowers the energy barrier for crystallization of its amorphous counterpart. This fact may

636   cause crystallization in the particles, leading to physical instability.

637   The surface compositions of the spray-dried particles measured by TOF-SIMS are shown in Figure 11,

638   with red and blue representing leucine and trehalose molecules, respectively. As expected, the average

639   leucine surface composition increased by increasing the leucine feed fraction from 10 to 40%. It can be

640   seen in all three cases that smaller particles had more trehalose on the surface than larger particles,

641   confirming the previous remarks on size-dependency of the particle morphology.

642   The pixel-average surface compositions of the spray-dried leucine/trehalose particles from the TOF-SIMS

643   spectra are plotted versus the bulk composition in Figure 12. These pixel-average values are presented for

644   the whole powder, and for small, medium and large particle fractions. The error bars for the total averages

645   are equal to the standard deviation of the pixel fractions of the whole frame. The total average leucine

646   surface coverage is seen to increase with leucine mass fraction. On average, 23% (mass basis) of the

647   particles are covered by leucine at a mass fraction of 10%, compared to the 48% coverage at a mass

648   fraction of 40%. It is also evident from these results that large particles have more leucine coverage than

649   small particles in all cases. It is likely that these small particles are composed of mostly amorphous

650   leucine with some small crystallinity, even for the case with the highest leucine mass fraction

651   (SD50T60L40). This can be deduced from the fact that the surface coverage of the small leucine particles

652   is smaller than even the bulk leucine fraction. This means that for these particles, the surface was enriched

653   by trehalose not leucine, due to the larger Péclet number of trehalose compared to leucine in molecular

654   form. Thus, there is no evidence of crystal growth. These small particles comprise only a very small mass

655   fraction of the total powder. Hence, their effect on the crystallinity measurements using the Raman

656   instrument are minimal. Nevertheless, it cannot be ruled out that the presence of even a small quantity of

657   amorphous leucine in the powder can potentially hinder the long-term physical stability of the product in

658   the form of both dry powder and suspension pressurized metered-dose inhalers (pMDIs).

659   In order to further interpret the phenomena explained above, the available time for leucine crystallization

660   versus the initial droplet diameter of the spray-dried powder is shown in Figure 13. As opposed to the

661   precipitation window explained in equation (7), here the available time for crystallization was defined

662   more precisely as the time for trehalose to reach a concentration of 830 mg/mL, less the time for leucine

663   to reach a critical supersaturation of 3.5. Assuming a logarithmic normal distribution with a mass median

664   diameter of 8 µm and an approximate geometric standard deviation of 2.2 for the atomized droplets, the

665    $d_{0,50}$, $d_{0,16}$ and $d_{0,84}$ are also indicated by the vertical grey lines. It is evident from these data that the time

666   available for crystallization increases sharply with increasing initial droplet diameter in all cases.

667   Assuming a particle density of 1000 mg/mL and a feed concentration of 50 mg/mL, equation (1) gives

668   initial droplet diameters smaller than 2.7 µm for solid particles smaller than 1 µm. Hence, for these

669   particles the time available for leucine crystallization is less than 1 ms. The difference in crystallization

670   times is the reason behind the large differences observed in the morphologies, leucine surface coverage

671   and possibly the crystallinity of the polydisperse particles. The crystallization windows of a sample case

672   for the CK-EDB and the droplet chain instrument are also shown in Figure 13 as the individual data

673   points. It is apparent from these calculated values that for both of these large droplets enough time is

674   available for complete crystallization of leucine, hence their similar behavior.
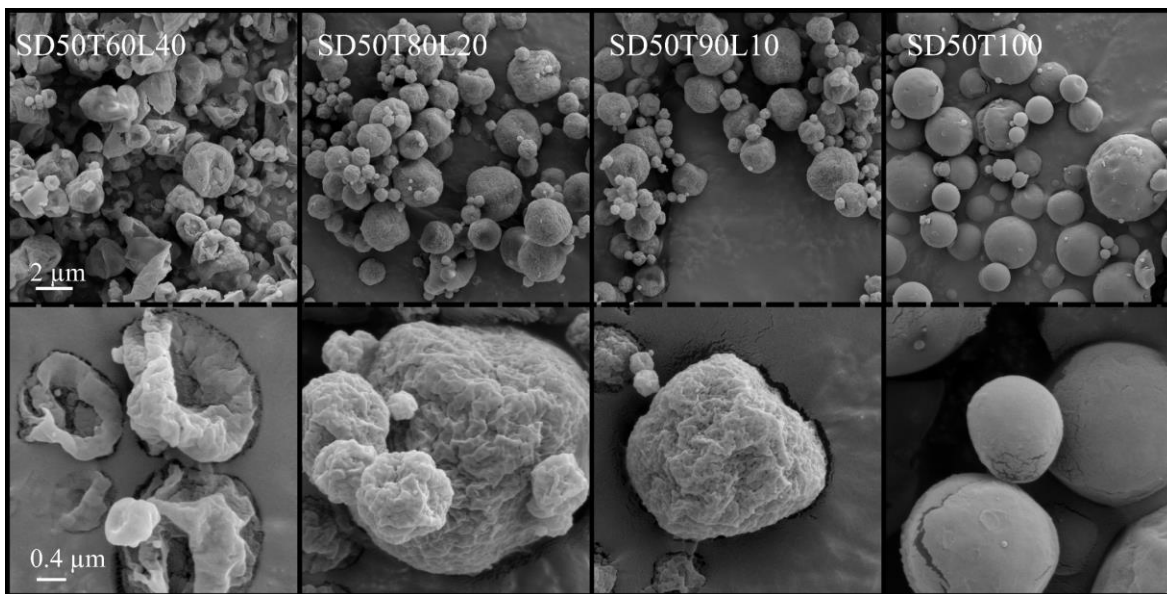
675

676   **Figure 9** SEM micrographs of the spray-dried leucine/trehalose particles dried at an inlet temperature of

677   75 °C. The scale bars apply to each row, and each column is of the same formulation. A label such as

678   SDαTβLγ means the spray-dried formulation had a total feed concentration of α with trehalose and

679   leucine mass fractions of β and γ, respectively.
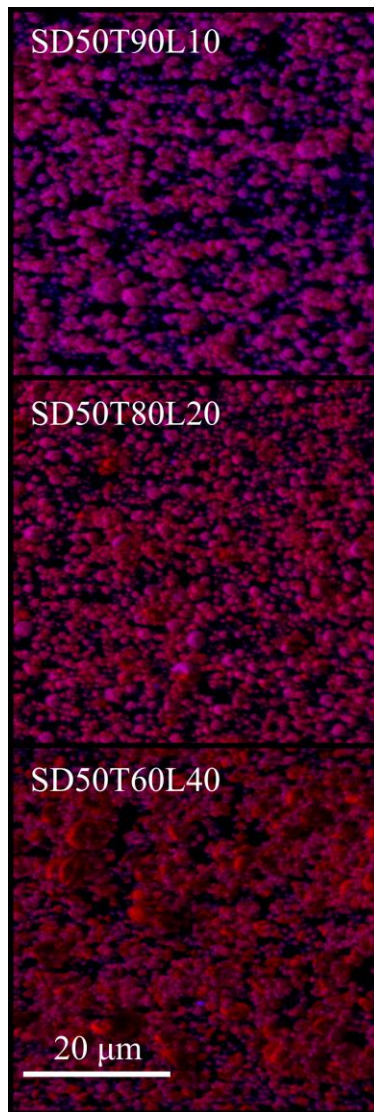
680
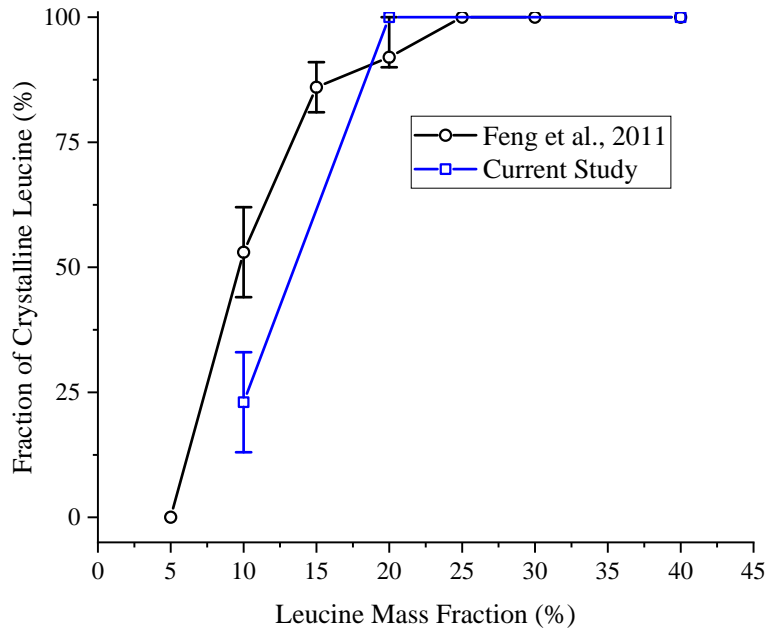
**Figure 10** The fractions of crystalline leucine in spray-dried leucine/trehalose particles. The drying

temperature was 75 °C in both studies, but the total feed concentrations were different.

683

Figure 11 The surface compositions of the spray-dried leucine/trehalose particles from the TOF-SIMS measurements. Red represents leucine molecules and blue represents trehalose. The scale bar applies to all three images. A label such as SDαTβLγ means the spray-dried formulation had a total feed concentration of α with trehalose and leucine mass fractions of β and γ, respectively.

688
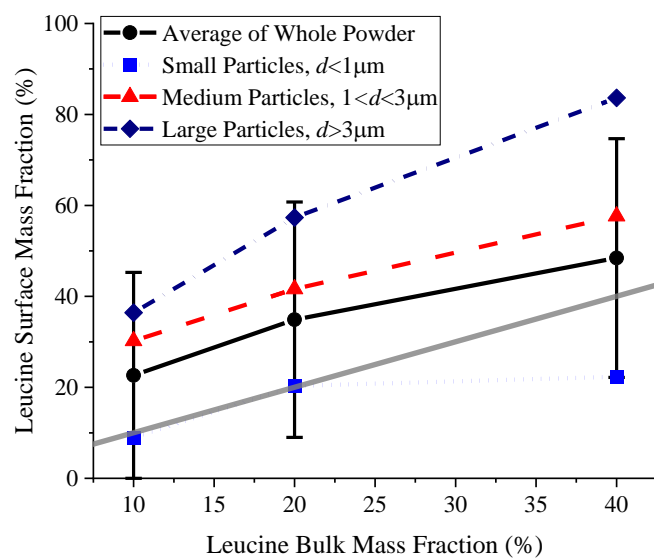
Figure 12 The pixel-average surface compositions of the spray-dried leucine/trehalose particles from the

TOF-SIMS spectra. The total feed concentration was 50 mg/mL and the drying temperature was 75 °C for

all cases. The grey line is the identity line (x=y).

692

693
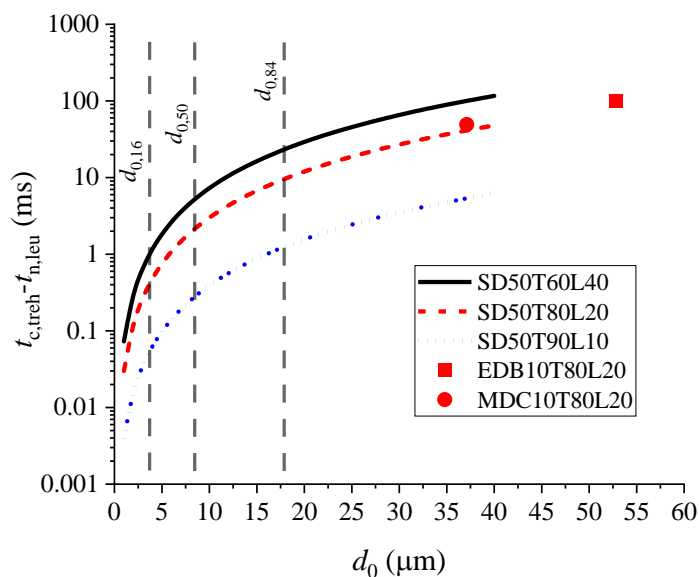
Figure 13 The available time for crystallization of leucine based on the difference between the time for trehalose to solidify and the time for leucine to reach the critical supersaturation, as a function of the initial droplet diameter. The curves apply to the spray-dried samples (drying temperature of 75 °C) accompanied by the vertical grey lines representing the approximate atomized droplet size distribution. The two individual data points represent a sample case of the electrodynamic balance and the droplet chain instruments (drying temperature of 20 °C).

700

701   3.4.   Application to Formulation Design

702   Based on the data available in the literature and the results obtained from the experiments conducted in

703   this study, it is possible to design and analyze spray-dried particles containing leucine as a dispersibility

704   enhancer. Such an approach has the potential to greatly reduce the number of experimental iterations

705   required in the design of a spray-dried platform containing other excipients and actives intended for

706   pulmonary delivery. The same framework may be used for other crystallizing components if the critical

707   parameters are determined in a similar fashion.

708   A dispersibility enhancing excipient needs to attain enough surface coverage on the final particle to have

709   the desired effects. If the solidification time of another excipient, τ_c, which is not intended to be on the

710   particle surface, is smaller, it will be faster to precipitate, leading to a higher surface composition. Hence,

711   the shell former should have the smallest τ_c compared to other excipients for maximum surface coverage.

712   For a crystallizing component, such as leucine, the dimensionless time to reach critical supersaturation,

713   τ_n, is also important. If the other excipients solidify near the surface before the crystallizing component

714   can nucleate, then the shell former is expected to remain partially or completely amorphous. This is

715   because in this case the shell former molecules do not have enough mobility to fit into a crystal lattice or

716   reach the surface in the fast time scales of spray drying. For example, in the present case of leucine and

717   trehalose particles, if trehalose reaches its critical concentration before leucine can nucleate, i.e. $\tau_{c,treh} <$

718    $\tau_{n,leu}$, leucine will most likely be completely amorphous and will not have a very high surface coverage.

719   On the other hand, if $\tau_{n,leu} < \tau_{c,treh} < \tau_{c,leu}$, then leucine is expected to be partially amorphous with low

720   surface coverage. Lastly, if $\tau_{c,leu} << \tau_{c,treh}$, then most of leucine should have had enough time to

721   crystallize and cover the surface. It should be noted that even if leucine does not crystallize in a

722   formulation, it can still lower the surface energy of the particles due to its surface activity and molecular

723   surface enrichment.

724   These considerations can be extended to other systems containing more excipients and APIs in order to

725   design the formulation in such a way as to ensure optimal surface coverage by the shell former.

726

4. Conclusion

728   This study demonstrates that the combination of the results obtained from an electrodynamic balance, a

729   monodisperse droplet chain instrument, and a spray dryer holds great potential for the study of particle

730   formation of different excipients and APIs in spray-dried microparticles. These results may greatly reduce

731   the experimental efforts necessary in the early stages of the formulation design of a solid dosage form.

732   It was confirmed that the surface accumulation of leucine is based on nucleation and crystal growth and

733   that the presence of other material in high concentrations can decrease surface enrichment due to

734   crystallization. It was also observed that the surface coverage and solid phase of leucine, as a crystalline

735   dispersibility enhancer, can be dependent on the initial droplet diameter due to the amount of time

736   required to nucleate, crystallize and form a shell. This fact has important implications for scale-up and

737   optimization of manufacturing parameters in these systems. A critical supersaturation ratio at which

738   leucine can spontaneously nucleate was also determined theoretically and supported by experimentation.

739   Furthermore, critical solidification and shell formation times were obtained for trehalose and leucine

740   using the single-particle experiments, which can be used in the formulation design of systems containing

741   these excipients to estimate leucine crystallinity and the extent of its surface coverage. The same

742   methodology can be applied for other crystallizing excipients or actives.

743

747

References

Baldelli, A., Boraey, M.A., Nobes, D.S., Vehring, R., 2015. Analysis of the Particle Formation Process of Structured Microparticles. Mol. Pharm. 12, 2562–2573. https://doi.org/10.1021/mp500758s

Baldelli, A., Power, R.M., Miles, R.E.H., Reid, J.P., Vehring, R., 2016. Effect of crystallization kinetics on the properties of spray dried microparticles. Aerosol Sci. Technol. 50, 693–704. https://doi.org/10.1080/02786826.2016.1177163

Baldelli, A., Vehring, R., 2016a. Analysis of cohesion forces between monodisperse microparticles with rough surfaces. Colloids Surfaces A Physicochem. Eng. Asp. 506, 179–189. https://doi.org/https://doi.org/10.1016/j.colsurfa.2016.06.009

Baldelli, A., Vehring, R., 2016b. Control of the radial distribution of chemical components in spray-dried crystalline microparticles. Aerosol Sci. Technol. 50, 1130–1142. https://doi.org/10.1080/02786826.2016.1216941

Boraey, M.A., Hoe, S., Sharif, H., Miller, D.P., Lechuga-Ballesteros, D., Vehring, R., 2013. Improvement of the dispersibility of spray-dried budesonide powders using leucine in an ethanol–water cosolvent system. Powder Technol. 236, 171–178. https://doi.org/10.1016/j.powtec.2012.02.047

Boraey, M.A., Vehring, R., 2014. Diffusion controlled formation of microparticles. J. Aerosol Sci. 67, 131–143. https://doi.org/10.1016/j.jaerosci.2013.10.002

Carrigy, N., Vehring, R., 2019. Engineering Stable Spray-Dried Biologic Powder for Inhalation, in: Hickey, A.J., da Rocha, S.R. (Eds.), Pharmaceutical Inhalation Aerosol Technology. CRC Press, Boca Raton, Florida, pp. 291–236.

Carrigy, N.B., Ordoubadi, M., Liu, Y., Melhem, O., Barona, D., Wang, H., Milburn, L., Ruzycki, C.A., Finlay, W.H., Vehring, R., 2019. Amorphous pullulan trehalose microparticle platform for respiratory delivery. Int. J. Pharm. 563, 156–168. https://doi.org/10.1016/j.ijpharm.2019.04.004

Dabbagh, A., Abu Kasim, N.H., Yeong, C.H., Wong, T.W., Abdul Rahman, N., 2018. Critical Parameters for Particle-Based Pulmonary Delivery of Chemotherapeutics. J. Aerosol Med. Pulm. Drug Deliv. 31, 139–154. https://doi.org/10.1089/jamp.2017.1382

Davies, J.F., Haddrell, A.E., Reid, J.P., 2012. Time-Resolved Measurements of the Evaporation of Volatile Components from Single Aerosol Droplets. Aerosol Sci. Technol. 46, 666–677. https://doi.org/10.1080/02786826.2011.652750

de Souza Lima, R., Ré, M.-I., Arlabosse, P., 2020. Drying droplet as a template for solid formation: A review. Powder Technol. 359, 161–171. https://doi.org/10.1016/j.powtec.2019.09.052

Eedara, B.B., Rangnekar, B., Doyle, C., Cavallaro, A., Das, S.C., 2018. The influence of surface active L-leucine and 1,2-dipalmitoyl-sn-glycero-3-phosphatidylcholine (DPPC) in the improvement of aerosolization of pyrazinamide and moxifloxacin co-spray dried powders. Int. J. Pharm. 542, 72–81. https://doi.org/10.1016/j.ijpharm.2018.03.005

Feng, A.L., Boraey, M.A., Gwin, M.A., Finlay, P.R., Kuehl, P.J., Vehring, R., 2011. Mechanistic models facilitate efficient development of leucine containing microparticles for pulmonary drug delivery. Int. J. Pharm. 409, 156–163. https://doi.org/10.1016/j.ijpharm.2011.02.049

Finlay, W.H., 2019. The Mechanics of Inhaled Pharmaceutical Aerosols: an Introduction, 2nd ed. Elsevier.

788 Fu, N., Woo, M.W., Chen, X.D., 2012. Single Droplet Drying Technique to Study Drying Kinetics
789   Measurement and Particle Functionality: A Review. Dry. Technol. 30, 1771–1785.
790   https://doi.org/10.1080/07373937.2012.708002

791 Galmarini, M.V., Baeza, R., Sanchez, V., Zamora, M.C., Chirife, J., 2011. Comparison of the viscosity of
792   trehalose and sucrose solutions at various temperatures: Effect of guar gum addition. LWT - Food
793   Sci. Technol. 44, 186–190. https://doi.org/10.1016/J.LWT.2010.04.021

794 Gliński, J., Chavepeyer, G., Platten, J.-K., 2000. Surface properties of aqueous solutions of l-leucine.
795   Biophys. Chem. 84, 99–103. https://doi.org/10.1016/S0301-4622(99)00150-7

796 Gregson, F.K.A., Ordoubadi, M., Miles, R.E.H., Haddrell, A.E., Barona, D., Lewis, D., Church, T.,
797   Vehring, R., Reid, J.P., 2019. Studies of competing evaporation rates of multiple volatile
798   components from a single binary-component aerosol droplet. Phys. Chem. Chem. Phys.
799   https://doi.org/10.1039/C9CP01158G

800 Gregson, F.K.A., Robinson, J.F., Miles, R.E.H., Royall, C.P., Reid, J.P., 2020. Drying and Crystallization
801   of Evaporating Sodium Nitrate Aerosol Droplets. J. Phys. Chem. B 124, 6024–6036.
802   https://doi.org/10.1021/acs.jpcb.0c04079

803 Griesing, M., Grosshans, H., Hellwig, T., Sedelmayer, R., Gopireddy, S.R., Pauer, W., Gutheil, E.,
804   Moritz, H.-U., 2016. Influence of Air Humidity on the Particle Formation of Single Mannitol-Water
805   Droplets during Drying. Chemie Ing. Tech. 88, 929–936. https://doi.org/10.1002/cite.201500087

806 Haddrell, A., Rovelli, G., Lewis, D., Church, T., Reid, J., 2019. Identifying time-dependent changes in the
807   morphology of an individual aerosol particle from its light scattering pattern. Aerosol Sci. Technol.
808   1–18. https://doi.org/10.1080/02786826.2019.1661351

809 He, G., Bhamidi, V., Tan, R.B.H., Kenis, P.J.A., Zukoski, C.F., 2006. Determination of Critical
810   Supersaturation from Microdroplet Evaporation Experiments. Cryst. Growth Des. 6, 1175–1180.
811   https://doi.org/10.1021/cg050681f

812 Healy, A.M., Amaro, M.I., Paluch, K.J., Tajber, L., 2014. Dry powders for oral inhalation free of lactose
813   carrier particles. Adv. Drug Deliv. Rev. 75, 32–52. https://doi.org/10.1016/j.addr.2014.04.005

814 Held, C., Cameretti, L.F., Sadowski, G., 2011. Measuring and Modeling Activity Coefficients in Aqueous
815   Amino-Acid Solutions. Ind. Eng. Chem. Res. 50, 131–141. https://doi.org/10.1021/ie100088c

816 Hennet, L., Cristiglio, V., Kozaily, J., Pozdnyakova, I., Fischer, H.E., Bytchkov, A., Drewitt, J.W.E.,
817   Leydier, M., Thiaudière, D., Gruner, S., Brassamin, S., Zanghi, D., Cuello, G.J., Koza, M., Magazù,
818   S., Greaves, G.N., Price, D.L., 2011. Aerodynamic levitation and laser heating: Applications at
819   synchrotron and neutron sources. Eur. Phys. J. Spec. Top. 196, 151–165.
820   https://doi.org/10.1140/epjst/e2011-01425-0

821 Hoe, S., Ivey, J.W., Boraey, M.A., Shamsaddini-Shahrbabak, A., Javaheri, E., Matinkhoo, S., Finlay,
822   W.H., Vehring, R., 2014. Use of a Fundamental Approach to Spray-Drying Formulation Design to
823   Facilitate the Development of Multi-Component Dry Powder Aerosols for Respiratory Drug
824   Delivery. Pharm. Res. 31, 449–465. https://doi.org/10.1007/s11095-013-1174-5

825 Lechanteur, A., Evrard, B., 2020. Influence of Composition and Spray-Drying Process Parameters on
826   Carrier-Free DPI Properties and Behaviors in the Lung: A review. Pharmaceutics 12, 55.
827   https://doi.org/10.3390/pharmaceutics12010055

828 Lechuga-Ballesteros, D., Charan, C., Stults, C.L.M., Stevenson, C.L., Miller, D.P., Vehring, R., Tep, V.,
829   Kuo, M., 2008. Trileucine Improves Aerosol Performance and Stability of Spray-Dried Powders for
830   Inhalation. J. Pharm. Sci. 97, 287–302. https://doi.org/10.1002/jps.21078

831 Lechuga-Ballesteros, D., Hoe, S., Maynor, B.W., 2019. Particle Engineering Technology for Inhaled
832   Therapies, in: Hickey, A.J., da Rocha, S.R.P. (Eds.), Pharmaceutical Inhalation Aerosol Technology.
833   CRC Press, Boca Raton, Florida, pp. 349–361. https://doi.org/10.1201/9780429055201

834 Li, L., Sun, S., Parumasivam, T., Denman, J.A., Gengenbach, T., Tang, P., Mao, S., Chan, H.-K., 2016. l -
835   Leucine as an excipient against moisture on in vitro aerosolization performances of highly
836   hygroscopic spray-dried powders. Eur. J. Pharm. Biopharm. 102, 132–141.
837   https://doi.org/10.1016/j.ejpb.2016.02.010

838 Mah, P.T., O'Connell, P., Focaroli, S., Lundy, R., O'Mahony, T.F., Hastedt, J.E., Gitlin, I., Oscarson, S.,
839   Fahy, J. V., Healy, A.M., 2019. The use of hydrophobic amino acids in protecting spray dried
840   trehalose formulations against moisture-induced changes. Eur. J. Pharm. Biopharm. 144, 139–153.
841   https://doi.org/10.1016/j.ejpb.2019.09.014

842 Mangal, S., Meiser, F., Tan, G., Gengenbach, T., Denman, J., Rowles, M.R., Larson, I., Morton, D.A.V.,
843   2015. Relationship between surface concentration of l-leucine and bulk powder properties in spray
844   dried formulations. Eur. J. Pharm. Biopharm. 94, 160–169.
845   https://doi.org/10.1016/j.ejpb.2015.04.035

846 Marty, G., Tsapis, N., 2008. Monitoring the buckling threshold of drying colloidal droplets using water-
847   ethanol mixtures. Eur. Phys. J. E 27, 213. https://doi.org/10.1140/epje/i2008-10375-6

848 MATLAB, 2019. version 9.6.0 (R2019a). The MathWorks Inc., Natick, Massachusetts.

849 Mondragon, R., Hernandez, L., Enrique Julia, J., Carlos Jarque, J., Chiva, S., Zaitone, B., Tropea, C.,
850   2011. Study of the drying behavior of high load multiphase droplets in an acoustic levitator at high
851   temperature conditions. Chem. Eng. Sci. 66, 2734–2744. https://doi.org/10.1016/j.ces.2011.03.033

852 Mullin, J.W., 2001. Nucleation, in: Crystallization. Elsevier, Oxford, pp. 181–215.
853   https://doi.org/10.1016/B978-075064833-2/50007-3

854 Muramoto, S., Brison, J., Castner, D.G., 2012. Exploring the Surface Sensitivity of TOF-Secondary Ion
855   Mass Spectrometry by Measuring the Implantation and Sampling Depths of Bi n and C 60 Ions in
856   Organic Films. Anal. Chem. 84, 365–372. https://doi.org/10.1021/ac202713k

857 Nicholas, M., Josefson, M., Fransson, M., Wilbs, J., Roos, C., Boissier, C., Thalberg, K., 2020.
858   Quantification of surface composition and surface structure of inhalation powders using TOF-SIMS.
859   Int. J. Pharm. 587, 119666. https://doi.org/10.1016/j.ijpharm.2020.119666

860 Nuzzo, M., Millqvist-Fureby, A., Sloth, J., Bergenstahl, B., 2015. Surface Composition and Morphology
861   of Particles Dried Individually and by Spray Drying. Dry. Technol. 33, 757–767.
862   https://doi.org/10.1080/07373937.2014.990566

863 Ordoubadi, M., Gregson, F., Finlay, W.H., Vehring, R., Reid, J.P., 2018. Interaction of evaporating
864   multicomponent microdroplets with humid environments, in: Respiratory Drug Delivery.

865 Ordoubadi, M., Gregson, F.K.A., Melhem, O., Barona, D., Miles, R.E.H., D'Sa, D., Gracin, S., Lechuga-
866   Ballesteros, D., Reid, J.P., Finlay, W.H., Vehring, R., 2019. Multi-Solvent Microdroplet
867   Evaporation: Modeling and Measurement of Spray-Drying Kinetics with Inhalable Pharmaceutics.
868   Pharm. Res. 36, 100. https://doi.org/10.1007/s11095-019-2630-7

869 Rovelli, G., Miles, R.E.H., Reid, J.P., Clegg, S.L., 2016. Accurate Measurements of Aerosol Hygroscopic
870   Growth over a Wide Range in Relative Humidity. J. Phys. Chem. A 120, 4376–4388.
871   https://doi.org/10.1021/acs.jpca.6b04194

872 Schneider, C.A., Rasband, W.S., Eliceiri, K.W., 2012. NIH Image to ImageJ: 25 years of image analysis.

873   Nat. Methods 9, 671–675. https://doi.org/10.1038/nmeth.2089

874 Seville, P.C., Learoyd, T.P., Li, H.-Y., Williamson, I.J., Birchall, J.C., 2007. Amino acid-modified spray-
875   dried powders with enhanced aerosolisation properties for pulmonary drug delivery. Powder
876   Technol. 178, 40–50. https://doi.org/10.1016/j.powtec.2007.03.046

877 Vehring, R., 2008. Pharmaceutical Particle Engineering via Spray Drying. Pharm. Res. 25, 999–1022.
878   https://doi.org/10.1007/s11095-007-9475-1

879 Vehring, R., Foss, W.R., Lechuga-Ballesteros, D., 2007. Particle formation in spray drying. J. Aerosol
880   Sci. 38, 728–746. https://doi.org/10.1016/j.jaerosci.2007.04.005

881 Wang, H., Barona, D., Oladepo, S., Williams, L., Hoe, S., Lechuga-Ballesteros, D., Vehring, R., 2017.
882   Macro-Raman spectroscopy for bulk composition and homogeneity analysis of multi-component
883   pharmaceutical powders. J. Pharm. Biomed. Anal. 141, 180–191.
884   https://doi.org/10.1016/j.jpba.2017.04.003

885 Wang, H., Nobes, D.S., Vehring, R., 2019. Particle Surface Roughness Improves Colloidal Stability of
886   Pressurized Pharmaceutical Suspensions. Pharm. Res. 36, 43. https://doi.org/10.1007/s11095-019-
887   2572-0

888 Weber, J.K.R., Tamalonis, A., Benmore, C.J., Alderman, O.L.G., Sendelbach, S., Hebden, A.,
889   Williamson, M.A., 2016. Aerodynamic levitator for in situ x-ray structure measurements on high
890   temperature and molten nuclear fuel materials. Rev. Sci. Instrum. 87, 073902.
891   https://doi.org/10.1063/1.4955210

892 Yalkowsky, S.H., He, Y., Jain, P., 2019. Handbook of aqueous solubility data, Second. ed. CRC press,
893   Boca Raton, Florida.

894 Yang, F., Liu, X., Wang, W., Liu, C., Quan, L., Liao, Y., 2015. The effects of surface morphology on the
895   aerosol performance of spray-dried particles within HFA 134a based metered dose formulations.
896   Asian J. Pharm. Sci. 10, 513–519. https://doi.org/10.1016/j.ajps.2015.07.006

897 Yaws, C.L., 2010. Yaws' Thermophysical Properties of Chemicals and Hydrocarbons (Electronic
898   Edition) [WWW Document]. URL https://app.knovel.com/hotlink/toc/id:kpYTPCHE02/yaws-
899   thermophysical-properties/yaws-thermophysical-properties (accessed 11.14.19).